

DARB-Splatting: Generalizing Splatting with Decaying Anisotropic Radial Basis Functions

Hashiru Pramuditha^{1,*} Vinasirajan Viruthshaan^{1,*} Vishagar Arunan^{1,*} Saeedha Nazar^{1,*}
 Sameera Ramasinghe² Simon Lucey² Ranga Rodrigo^{1,†}
¹University of Moratuwa ²University of Adelaide

Abstract

Splatting-based 3D reconstruction methods have gained popularity with the advent of 3D Gaussian Splatting, efficiently synthesizing high-quality novel views. These methods commonly resort to using exponential family functions, such as the Gaussian function, as reconstruction kernels due to their anisotropic nature, ease of projection, and differentiability in rasterization. However, the field remains restricted to variations within the exponential family, leaving generalized reconstruction kernels largely underexplored, partly due to the lack of easy integrability in 3D to 2D projections. In this light, we show that a class of decaying anisotropic radial basis functions (DARBFs), which are non-negative functions of the Mahalanobis distance, supports splatting by approximating the Gaussian function’s closed-form integration advantage. With this fresh perspective, we demonstrate varying performances across selected DARB reconstruction kernels, achieving comparable training convergence and memory footprints, with on-par PSNR, SSIM, and LPIPS results.

1. Introduction

3D Gaussian Splatting (3DGS) [11] has gained widespread attention in 3D reconstruction due to its state-of-the-art (SOTA) performance and real-time rendering capabilities. Since then, 3DGS has seen expanding industrial applications, spanning 3D web viewers, 3D scanning, VR platforms, and more [31]. As demand continues to rise, optimizing models for efficiency becomes crucial. Given this, the need for resource-efficient approaches in 3DGS is becoming increasingly important.

Splatting plays a pivotal role in modern 3D reconstruction, enabling the representation of 3D points without relying on surface meshes. 3DGS, which is a splatting-based technique, represents these 3D points as a dynamically den-

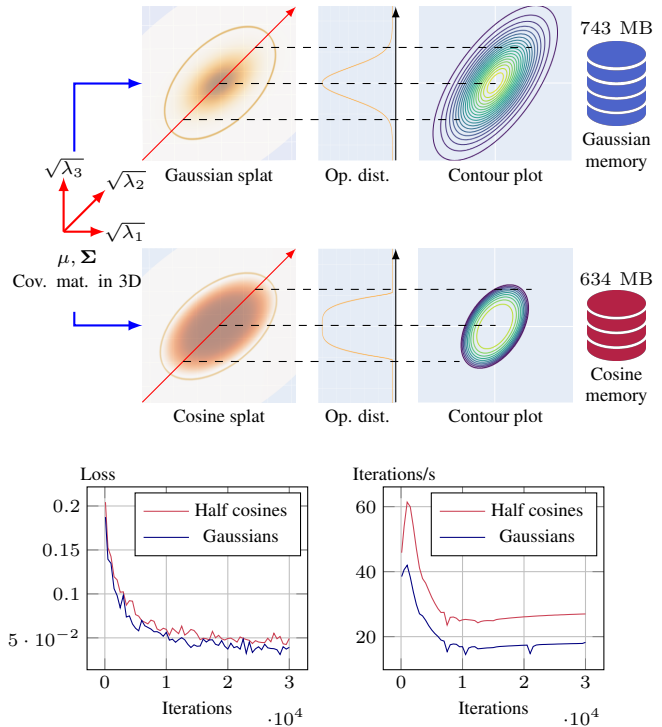


Figure 1. This figure compares two different splat functions—Gaussian and cosine (specifically, half-cosine)—initialized for the same 3D covariance matrix Σ , confined by eigenvalues $\lambda_1, \lambda_2, \lambda_3$. Half-cosine functions, defined as $\cos\left(\frac{d_M^2}{\xi}\right)$ for $d_M^2 < \frac{\xi\pi}{2}$ where $\xi > 0$, have finite support and exhibit effective reconstruction performance comparable to Gaussians. Notably, this non-exponential-based approach enhances training speed by 34% and reduces memory usage by 15%, providing a more efficient alternative.

sified radiance field of 3D Gaussian primitives (ellipsoids) that act as reconstruction kernels. In theory, these ellipsoids are integrated along the projection direction onto the 2D image plane, resulting in 2D Gaussians or splats, a function known as the footprint function or splatting function. This process exploits an interesting property of Gaussians: 2×2 covariance matrix of the 2D Gaussian can be obtained by

*These authors contributed equally to this work.

†Correspondence: ranga@uom.lk

skipping the third row and column of the 3×3 covariance matrix of the 3D Gaussian [82]. This bypasses costly integration and efficiently simplifies the rendering in practical implementation. The footprint function then models the spread of each splat’s opacity, eventually contributing to the final pixel color. This Gaussian-based blending effect—a smooth, continuous interpolation between splats—inspires the method’s name, “3D Gaussian Splatting.” Numerous subsequent papers [6, 7, 30, 73, 78] build upon this principle, although still restricted to exponential family functions (*e.g.*, Gaussian functions) to spread each sample in image space.

Splatting methods depend on the mean (position) and covariance of 3D points, making them independent of the reconstruction kernel. However, existing work commonly resort to the Gaussian kernel, with some variations within the exponential family (*e.g.*, super-Gaussian [10], half-Gaussian [34], Gaussian-Hermite [77] kernels). However, classical signal processing and sampling theory establish that while Gaussians are useful, there exist other effective interpolators. In this paper we argue that the Gaussian function is not the only possible interpolator, especially when determining the pixel color, as in 3DGS. We see other functions outperforming them in various contexts, with a notable example being JPEG compression [58, 66], which leverages Discrete Cosine Transforms (DCTs) instead of Gaussians functions for image representation. Additionally, Saratchandran *et al.* [53] demonstrate that the sinc activation surpasses Gaussian activation in implicit neural representations [22, 25, 40, 60], while also suggesting several alternative activation functions. This raises the question: *Should splatting be limited only to Gaussians or the exponential family?* This remains an underexplored area in the community, partly because costly integration processes make it computationally inefficient to use functions outside of Gaussians.

To address these shortcomings, we generalize these kernels by introducing a broader class of functions: **Decaying Anisotropic Radial Basis Functions (DARBFs)**. These non-negative functions (*e.g.*, modified raised cosine, half-cosine, modular sinc functions) include, but are not limited to the exponential family. DARBFs support anisotropic behavior as they rely on the Mahalanobis distance and are differentiable, enabling differentiable rendering (Sec. 3.1). Our work demonstrates the potential of moving beyond Gaussians in optimizing splatting by showcasing how selected functions contribute to training speedups (*e.g.*, half-cosine function in Table 3 and Fig. 1) and memory efficiencies (*e.g.*, inverse quadratic function in Table 3), while maintaining on-par visual quality in novel views. In a field that often focuses on refining loss functions [16, 48], regularizing Gaussian parameters [24, 80], quantizing Gaussian parameters [42], we take a deeper approach by analyzing

the fundamental aspects of splatting. We replace the Gaussian itself by providing a plug-and-play replacement for kernels across the DARBF spectrum. Since our approach targets a fundamental aspect of the algorithm, it can be applied to all splatting methods built on top of the 3DGS framework.

To address the costly integration beyond Gaussians, we introduce a unique correction factor for different alternative kernels, while preserving the computational efficiency of 3DGS by approximating the Gaussian’s closed-form integration shortcut. This enables feasible splatting across the diverse functions in DARBFs.

To the best of our knowledge, our method represents one of the first modern generalizations expanding splatting to non-exponential functions, while maintaining comparable rendering quality, as splatting techniques scale to repetitive industrial applications, where computational savings are increasingly critical.

The contributions of our paper are as follows:

- We present a generalization of splatting functions using the DARBFs class, with Gaussians as a special case.
- Selected DARBF kernels offer up to 34% faster convergence and 15% lower memory use, with similar PSNR (Sec. 7).
- We propose an efficient method aided through a correction factor to retain Gaussian integration benefits for other kernels, supported by CUDA-based back-propagation codes (*Supplementary Material*).

2. Related Work

Radiance Field Representation. Early novel view synthesis (NVS) methods leveraged light fields [17, 33], later enhanced by SfM [59] and pipelines like COLMAP [54] to obtain sparse reconstructions from image collections [11, 18, 40, 79].

Neural Radiance Fields (NeRFs) [40] enabled photo-realistic novel view synthesis via volumetric rendering [1, 2, 12, 38, 39, 64], leading to extensive improvements in speed [15, 35, 36, 49, 50], supervision [9, 52], deformation [45–47, 81], and editing [37, 55, 63, 72]. In contrast, 3D Gaussian Splatting (3DGS) adopts point-based rendering using anisotropic splats and has rapidly impacted diverse domains [6, 8, 13, 23, 27, 32, 51, 56, 57, 62, 65, 69–71, 73, 75, 76]. Inspired by this, our method also uses point-based rendering but generalizes the opacity function beyond 3D Gaussians, introducing DARBFs as flexible image-space primitives, following ideas in [53].

Splatting. Splatting, introduced by Westover [67], enables point-based rendering of 3D data, such as sparse SfM

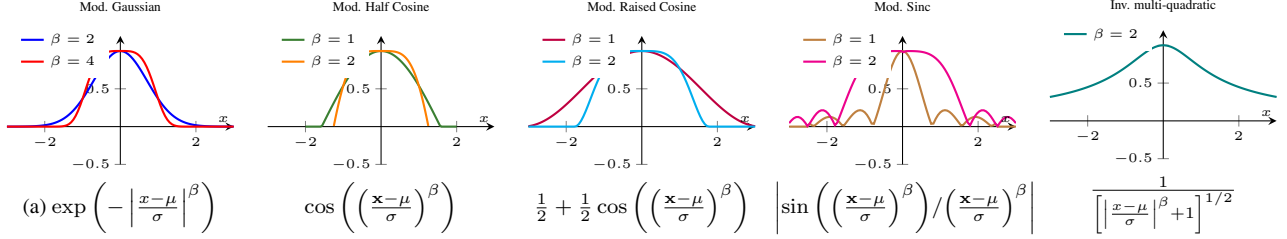


Figure 2. Overview of decaying anisotropic radial basis functions (DARBFs) shown with their respective 1D curves. These functions decay with distance and vary in their sensitivity to direction, making them effective for capturing anisotropic features in spatial data.

points [59] obtained from the COLMAP pipeline [54], without requiring mesh-like connectivity. Each particle’s position and shape are represented by a volume [67] that serves as a reconstruction kernel [82], which is projected onto the image plane through a “footprint function,” or “splat function,” to spread, or splat each particle’s intensity and color across a localized region. Early splatting techniques [68] commonly used spherical kernels for their radial symmetry to simplify calculations, although they struggled with perspective projections. To address this, elliptical kernels [68, 82], projecting elliptical footprints on the image plane were used to better approximate elongated features through anisotropic properties, ultimately enhancing rendering quality. Westover [68], further experimented with different reconstruction kernels, namely sinc, cone, Gaussian, and bilinear functions without focusing on a specific class of functions. EWA Splatting [82] further refined this approach by selecting a Gaussian reconstruction kernel in 3D, which projects as an elliptical Gaussian footprint on the image plane. This motivated 3DGS to adopt Gaussians. While effective, other anisotropic radial basis functions could serve as splats but remain underexplored.

Reconstruction Kernel Modifications. Although 3DGS claims SOTA performance, recent work has shown further improvements by refining the reconstruction kernel. For instance, GES [10] introduces the generalized exponential function, or the super Gaussian, by incorporating a learnable shape parameter for each point. Concurrent work such as 3D-HGS [34], splits the 3D Gaussian reconstruction kernel into two halves by modeling two different opacity distributions for the same splat. Similarly, 2DGH [77] extends the Gaussian function by incorporating Hermite polynomials into a Gaussian-Hermite reconstruction kernel. Meanwhile, triangle-based approaches [20], such as Triangle Splatting, influenced by [21], represent scenes using explicit triangle primitives that can be rendered as differentiable splats and optimized via end-to-end gradients. Similarly, customizing differentiable rasterizer for sparse voxel rendering [61] has been done to avoid popping artifacts in 3DGS [11] and to achieve high rendering frame rates. These methods achieve impressive results in terms of quality, training time and memory footprint, but

limiting to one particular class of reconstruction kernel. In our method, we preserve the general framework of point-based splatting while enhancing its expressiveness through Decaying Anisotropic Radial Basis Functions (DARBFs). By directly modifying the CUDA rasterizer, we enable a class of flexible, learnable reconstruction kernels without increasing memory overhead or requiring handcrafted priors, opening new avenues for future research.

Memory and Training Efficiency in Gaussian Splatting. The unstructured nature of Gaussians in 3DGS increases memory and training costs. Prior work addresses this with refined splatting [42], quantization via sensitivity-aware clustering [43], and adaptive spherical harmonics [44]. In contrast, we pursue kernel-level modifications, offering plug-and-replace compatibility with existing methods and opening a new path for optimization.

3. Preliminaries

3.1. DARB Functions

Radial basis functions (RBFs) serve as a fundamental class of mathematical functions, which depend on the distance from a center point. However, isotropic RBFs, which are radially symmetric, often fall short in capturing anisotropic features such as local geometric details that vary directionally, resulting in inaccuracies [5].

To address this issue, we use Anisotropic Radial Basis Functions (ARBFs) with a decaying nature, namely Decaying ARBFs (DARBFs), as we are interested in splatting, where splats decay spatially. For a particular point $\mathbf{x} \in \mathbb{R}^n$, the Mahalanobis distance (d_M), calculated from the center $\mu \in \mathbb{R}^n$ of a 3D DARBF, is given by:

$$d_M(\mathbf{x}; \mu, \Sigma) = [(\mathbf{x} - \mu)^T \Sigma^{-1} (\mathbf{x} - \mu)]^{\frac{1}{2}}, \quad (1)$$

where Σ denotes the covariance matrix. This radially dependent anisotropy supports smooth interpolation in 3 dimensional space ($n=3$), playing a pivotal role in 3D reconstruction.

3.2. Assessing DARBFs through 1D Simulations

As a simple proof of concept, we conducted 1D signal reconstruction simulations (Fig. 3). Our objective was to

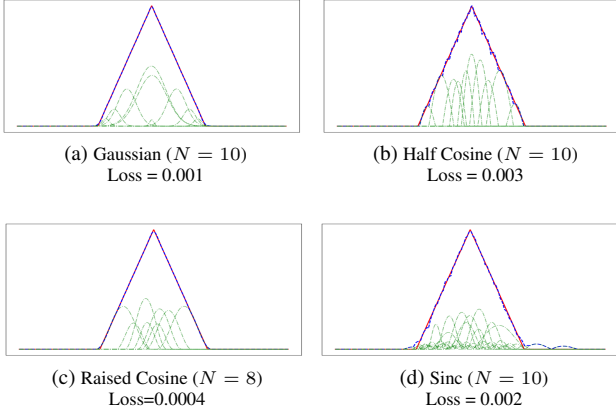


Figure 3. Simulations of 1D signal reconstruction through backpropagation across different DARBFs. Here, the target, reconstructed, and individual components are represented by red, blue, and green lines, respectively. We achieve competitive reconstruction results, validating our hypothesis that signals can be reconstructed using non-exponential kernels.

optimize the minimum number of primitives required for reconstructing a complex shape (e.g., triangle in this case) while fine-tuning the mean and variance values to minimize the loss, computed as the difference between the target and reconstructed functions. The simulation results indicate that, like Gaussian functions, non-exponential functions (DARBFs) can also achieve similar performance. Building on this insight, we incorporated selected DARBFs into the 3DGS algorithm with adjustments in domain constraints and backpropagation. We have provided a detailed analysis of these 1D simulations, including the results for reconstructing far more complex signals, in the *Supplementary Material*.

4. Methodology

We present DARBFs as a plug-and-play replacement for existing Gaussian kernels, offering improvements in training time and memory efficiency. The pipeline for DARB splatting is presented in Fig. 4.

Splatting-based reconstruction methods like 3DGS represent scenes by placing anisotropic Gaussian kernels at 3D points from an SfM pipeline, such as COLMAP. These kernels are transformed into the camera frame and projected onto 2D planes, creating splats. The pixel error between views and rasterized splats drives backpropagation to optimize the 3D Gaussians. This pipeline relies on four key properties: (1) differentiable rasterization, (2) anisotropic kernel behavior, (3) easy projectability, and (4) rapid decay.

A reconstruction kernel being a function of Mahalanobis distance d_M (Eq. 1), yields the first two properties [29]. Non-negative DARBFs, being rapidly decaying and a function of the Mahalanobis distance d_M [3], satisfy all four. In Sec. 4.1 we propose a method to approximate the projec-

tion of DARBFs, thereby satisfying the third property. The DARBF class can be explicitly defined as:

$$K(\mathbf{x}; \boldsymbol{\mu}, \boldsymbol{\Sigma}) = F(d_M(\mathbf{x}; \boldsymbol{\mu}, \boldsymbol{\Sigma})) \quad (2)$$

Here, $F: \mathbb{R}_{\geq 0} \rightarrow \mathbb{R}_{\geq 0}$ is a decaying, differentiable (finite- or fast-decay) radial profile.

4.1. DARB-Splatting

DARB Representation. Similar to 3DGS, we use the same parameterization to represent 3D DARBFs, as the Gaussian function is an instance of the DARBF class. In Table 1, we present the generic mathematical expressions of selected reconstruction kernel functions.

Function $F(d_M)$	Expression	Domain
Modified Gaussian	$\exp\left(-\frac{1}{\xi}(d_M)^\beta\right)$	$d_M \geq 0$
Modified half-cosine	$\cos\left(\frac{1}{\xi}(d_M)^\beta\right)$	$\frac{1}{\xi}(d_M)^\beta \leq \frac{\pi}{2}$
Modified raised cosine	$0.5 + 0.5 \cdot \cos\left(\frac{1}{\xi}(d_M)^\beta\right)$	$\frac{1}{\xi}(d_M)^\beta \leq n\pi$
Modified modular sinc	$\frac{\left \sin\left(\frac{1}{\xi}(d_M)^\beta\right)\right }{\frac{1}{\xi}(d_M)^\beta}$	$\frac{1}{\xi}(d_M)^\beta \leq \frac{(n+1)\pi}{2}$
Inv. multiquadric	$\frac{1}{\left[\frac{1}{\xi}(d_M)^2 + 1\right]^{\frac{1}{2}}}$	$d_M \geq 0$
Parabola	$1 - \frac{1}{\xi}(d_M)^2$	$\frac{1}{\xi}(d_M)^2 \leq 1$

Table 1. Overview of decaying anisotropic radial basis functions (DARBFs) $F(d_M)$ (Eq. 2) in 3D, with their limits (Sec. 4.1). Incorporating the Mahalanobis distance d_M (Eq. 1) enables precise control over each function’s main lobe, similar to 3D Gaussians, for capturing localized 3D features. The scaling factor $\xi(> 0)$ controls the spread of the covariance, while β controls the main lobe’s roll-off. Here, “modified” refers to the generalized version (e.g., modified half-cosine with generic β and half-cosine $\beta = 2$).

DARB Projection. To project 3D DARBs to DARB-splats, we use the method proposed by EWA Splatting [74, 82]. To project 3D mean ($\boldsymbol{\mu}$) in world coordinate system onto the 2D image plane, we use the conventional perspective projection. However, the same projection cannot be used to project the 3D covariance ($\boldsymbol{\Sigma}$) in world coordinates to the 2D covariance ($\boldsymbol{\Sigma}'_{2 \times 2}$) in image space. Hence, first, the 3D covariance ($\boldsymbol{\Sigma}$) is projected onto camera coordinate frame which results in a projected 3×3 covariance matrix ($\boldsymbol{\Sigma}'$). Given a viewing transformation W , the projected covariance matrix $\boldsymbol{\Sigma}'$ in camera coordinate frame can be obtained as $\boldsymbol{\Sigma}' = JW\Sigma W^T J^T$, where J denotes the Jacobian of the affine approximation of the projective transformation. Importantly, integrating a normalized 3D Gaussian along one coordinate axis results in a normalized 2D Gaussian itself. From that, the EWA Splatting [82] shows that the 2D covariance matrix ($\boldsymbol{\Sigma}'_{2 \times 2}$) of the 2D Gaussian can be easily obtained by taking the upper-left 2×2 sub-matrix of $\boldsymbol{\Sigma}'$, specifically by skipping the third row and third column (Eq. 4).

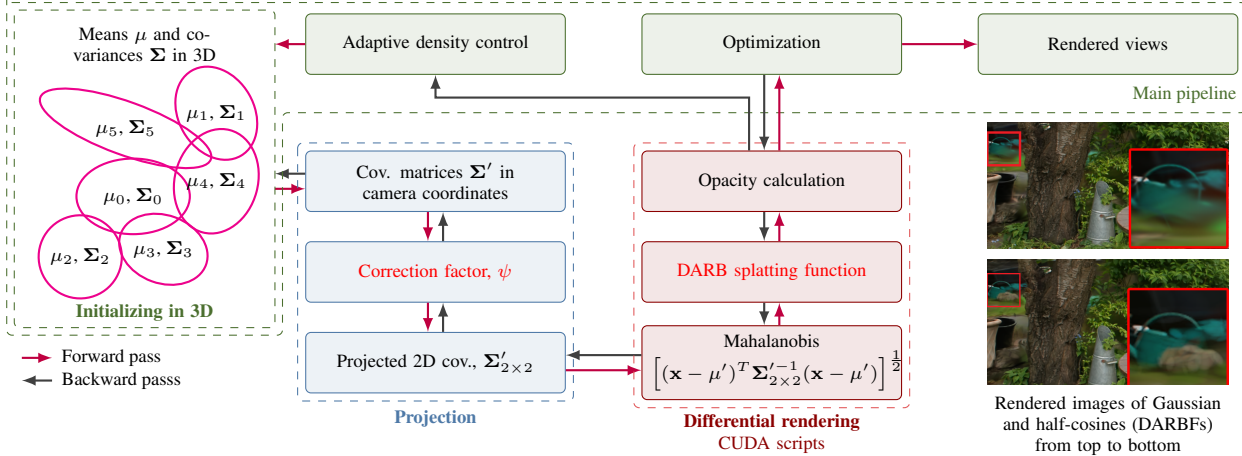


Figure 4. **Block diagram:** We use the standard optimization pipeline from 3DGS [11] with modifications, introducing a correction factor (ψ) to obtain the projected 2D covariance matrix ($\Sigma'_{2 \times 2}$) compatible with splatting for DARBFs within the existing framework. Our changes within the pipeline are highlighted in red text.

However, this sub-matrix shortcut applies only to Gaussian reconstruction kernels due to their inherent properties. Our core argument questions whether the integration described above is essential for the splatting process. While the Gaussian’s closed form integration is convenient, we propose interpreting the 3D covariance as a parameter that represents the 2D covariances from all viewing directions. When viewing a 3D Gaussian from a particular direction, we may think that the opacity would be distributed across the volume defined by each 3D Gaussian, and that alpha blending composites these overlapping volumes. But in reality, the 3D Gaussian is splatted into 2D and then only the opacity is distributed. In practice, however, the opacity distribution takes place after projecting 3D Gaussians to 2D splats. Thus, when a ray approaches, it only considers the Gaussian value derived from the 2D covariance of the splat. Additionally, the Gaussian value is not calculated for each point in the splat using **normalized** Gaussian function. As a simple example, consider two 3D Gaussians that are nearly identical in all properties except for the variance along the z-axis ($(\sigma'_z)^2$). When these two Gaussians are projected into 2D, we expect the 3D Gaussian with a higher σ'_z to have greater opacity values. In contrast, 3DGS yields a similar matrix ($\Sigma'_{2 \times 2}$) for both covariances, while exerting the same influence on opacity distribution along the splats. This further strengthens our argument for treating Σ' as a parameter to represent $\Sigma'_{2 \times 2}$.

Generally, integrating a 3D DARB along a certain axis does not yield the same DARBF in 2D, nor does it result in a closed-form solution. Therefore, we established the relationship between Σ' and $\Sigma'_{2 \times 2}$ for DARBFs through simulations. For clarity, we provide the derivations for the half-cosine splat here. Detailed derivations and corresponding CUDA scripts for selected DARBFs are provided in the

Supplementary Material. The 3D half-cosine kernels is as follows:

$$P_{i,j,k} = \begin{cases} \cos\left(\frac{\pi}{18}(d_M)^2\right), & \text{if } (d_M)^2 < 9, \\ 0, & \text{otherwise.} \end{cases} \quad (3)$$

where d_M (Eq. 1) is the Mahalanobis distance calculated between the kernel centers, retrieved from the point cloud as $P_{i,j,k}$ and the surrounding points in the 3D space. We then calculate the projected $\Sigma'_{2 \times 2}$ by summing values along a certain axis, similar to integrating along the same axis. As $\Sigma_{3 \times 3}$ is positive semi-definite to maintain strict decomposition, it is a symmetric matrix; $\Sigma'_{2 \times 2}$ are also symmetric.

$$\Sigma' = \begin{pmatrix} a & b & c \\ b & d & e \\ e & d & f \end{pmatrix} \rightarrow \psi \begin{pmatrix} a & b \\ b & d \end{pmatrix} = \Sigma'_{2 \times 2}. \quad (4)$$

Correction Factor (ψ). ψ accommodates our DARBFs to work efficiently with the existing 3DGS pipeline. We acknowledge that most of the functions are not closed under integration like Gaussians. To approximate this closed-form integration, we formulate an optimization problem that minimizes the difference between the covariance proposed by EWA Splatting [82], and the actual projected covariance, which we compute using Simpson’s rule [4] along an axis. We solve this problem using a multilayer perceptron (MLP) and integrate these precomputed weights into the CUDA pipeline.

Thus, incorporating the influence of ψ allows us to approximate the projected covariance matrix $\Sigma'_{2 \times 2}$, aligning it with the expected covariance and achieving comparable visual quality. However, this introduces a slight computational overhead. Therefore, we further evaluated this approach as a regression problem to approximate a pre-computed scalar ψ (derived in the *Supplementary Material*)

that can efficiently represent these weights without compromising visual performance. We have extensively ablated this.

Kernel	G	HC	RC	Sinc	IMQ	P
ξ	2	$18/\pi$	$2.5/\pi$	$3/\pi$	1	9
ψ	1	1.34	0.66	1.18	1.61	1.3

Table 2. Correction factor (ψ) values and selected scaling factor (ξ) values for DARBF primitives. Here, G: Gaussian, HC: Half-cosine, RC: Raised Cosine, Sinc: modular sines, IMQ: Inverse Multiquadric, and P: Parabolic functions (Table. 1).

Similarly, based on such empirical results, we modified the existing CUDA scripts of 3DGS to implement each DARBF separately with its respective ψ value to ensure comparable results. Additionally, we introduce a scaling factor ξ to match the extent of our function closely with the Gaussian, allowing a fair comparison of DARBF performance. Although Gaussian functions are spatially infinite, 3DGS [11] uses a bounded Gaussian to limit the opacity distribution in 2D, thereby reducing unnecessary processing time. For projected 2D splats, they calculate the maximum radius as $R = 3 \cdot \sqrt{\max\{\lambda_1, \lambda_2\}}$, where λ_1 and λ_2 denote the eigenvalues of the 2D covariance matrix $\Sigma'_{2 \times 2}$. Using this radius R , we obtain a similar extent for DARBFs as Gaussians with the help of ξ . Taking that into consideration, for $\xi = \frac{18}{\pi}$, the 2D half-cosine splat is defined as follows:

$$w = F(d_M) = \cos\left(\frac{1}{\xi}(d_M)^2\right), \quad (5)$$

$$d_M = [(\mathbf{x} - \mu)^T (\Sigma'_{2 \times 2})^{-1} (\mathbf{x} - \mu)]^{\frac{1}{2}}, \quad (6)$$

where $x \in \mathbb{R}^2$ is the position vector, $\mu' \in \mathbb{R}^2$ is the projected mean, and $\Sigma'_{2 \times 2} \in \mathbb{R}^{2 \times 2}$ represents the covariance matrix. Here, R_{cosine} will be $\frac{\sqrt{2\pi\xi \max(\lambda_1, \lambda_2)}}{2}$, indicating 100% extent, as we consider the entire central lobe. However, for a 2D Gaussian with an extent of 99.7% (up to three standard deviations), the radius R_{Gaussian} is given by $3\sqrt{\max(\lambda_1, \lambda_2)}$. To match the extent of both functions, we select $\xi (> 0)$ such that $\frac{\sqrt{2\pi\xi \max(\lambda_1, \lambda_2)}}{2} = 3\sqrt{\max(\lambda_1, \lambda_2)}$, which implies $\xi = \frac{18}{\pi}$.

Within this bounded region, we use our footprint function (Eq. 5) to model the opacity, similar to the approach in 3DGS. Following this, we apply alpha blending to determine the composite opacity [11, 74] for each pixel, eventually contributing to the final color of the 2D rendered image.

4.2. Backpropagation and Error Calculation

To support backpropagation (BP), we must account for the differentiability of DARBFs. As usual, the BP process begins with a loss function that combines the same losses discussed in the original work [11]: an \mathcal{L}_1 loss and an Structural Similarity Index Measure (SSIM) loss, which guide

the 3D DARBs to optimize its parameters.

$$\mathcal{L} = (1 - \lambda)\mathcal{L}_1 + \lambda\mathcal{L}_{\text{D-SSIM}} \quad (7)$$

where λ denotes each loss term’s contribution to the final image loss. After computing the loss, we perform back-propagation, where we explicitly modify the differentiable Gaussian rasterizer from 3DGS [11] to support respective gradient terms for each DARBF.

The following example demonstrates these modifications for the 3D half-cosine function (Eq. 5) with $\xi = \frac{18}{\pi}$.

$$\frac{dw}{d(x - \mu')} = F'(d_M) \frac{d(d_M)}{d(x - \mu')} \quad (8)$$

$$\frac{dw}{d((\Sigma'_{2 \times 2})^{-1})} = F'(d_M) \frac{d(d_M)}{d((\Sigma'_{2 \times 2})^{-1})} \quad (9)$$

Where

$$F'(d_M) = -\sin\left(\frac{(x - \mu')^T (\Sigma'_{2 \times 2})^{-1} (x - \mu')}{\xi}\right) \quad (10)$$

$$\frac{\partial d_M}{\partial (\Sigma'_{2 \times 2})^{-1}} = \frac{(x - \mu')(x - \mu')^T}{\xi}, \quad \frac{\partial d_M}{\partial (x - \mu')} = \frac{2(\Sigma'_{2 \times 2})^{-1}(x - \mu')}{\xi} \quad (11)$$

5. Experiments

Experimental Settings. We anchor our contributions on the recently *updated codebase* of 3DGS as of *October 2024* [11], adjusting the CUDA scripts to support a range of DARBFs. For a fair comparison, we use the same scenes as the 3DGS paper, including both bounded indoor and large outdoor environment scenes from various datasets [12, 19, 26]. We utilized the same COLMAP [54] initialization provided by the official dataset for all tests conducted to ensure fairness. Furthermore, we retained the original hyperparameters, adjusting only the opacity learning rate to 0.02 for improved results. All experiments and evaluations were conducted, and further verified on a single NVIDIA GeForce RTX 4090 GPU.

We compare our work with SOTA splatting-based methods that use exponential family reconstruction kernels, such as the *original 3DGS*, *updated codebase* of 3DGS, and GES [10] as benchmarks. We also evaluated the DARBFs using the standard and frequently used PSNR, LPIPS and SSIM metrics similar to these benchmarks (Table 3).

5.1. Quantitative Results and Discussion

Table 3 shows that different functions showcase different capabilities in terms of training and memory efficiency. We do not aim for superior reconstruction gains. However, results in Table 3 show that the modified raised cosine function ($\xi = \frac{2.5}{\pi}$) achieves modestly improved performance compared to Gaussians, particularly in LPIPS and SSIM metrics (visual comparisons are available in *Supplementary*

Function	Mip-NeRF 360					Tanks & Temples					Deep Blending				
	SSIM↑	PSNR↑	LPIPS↓	Train	Memory	SSIM↑	PSNR↑	LPIPS↓	Train	Memory	SSIM↑	PSNR↑	LPIPS↓	Train	Memory
3DGS (7k) [11]	0.770	25.60	0.279	4m 43s*	523 MB	0.767	21.20	0.28	5m 05s*	270 MB	0.875	27.78	0.317	3m 22s*	368 MB
3DGS (30K) [11]	0.815	27.21	0.214	30m 33s*	734 MB	0.841	23.14	0.183	19m 46s*	411 MB	0.903	29.41	0.243	26m 29s*	676 MB
GES [10]	0.794	26.91	0.250	19m 9s	377 MB	0.836	23.35	0.198	15m 26s*	222 MB	0.901	29.68	0.252	22m 44s*	399 MB
3DGS-updated (7K)	0.769	25.95	0.281	3m 24s	504 MB	0.781	21.78	0.261	2m 02s	293 MB	0.879	28.42	0.305	3m 14s	462 MB
3DGS-updated (30K)	0.813	27.45	0.218	19m 06s	633 MB	0.847	23.77	0.173	11m 24s	371 MB	0.901	29.66	0.242	20m 12s	742 MB
Raised cosine (7K)	0.773	26.01	0.273	3m 13s	513 MB	0.788	21.88	0.251	1m 59s	304 MB	0.882	28.47	0.300	2m 57s	401 MB
Raised cosine (30K)	0.813	27.45	0.214	19m 36s	645 MB	0.851	23.64	0.166	12m 06s	364 MB	0.901	29.63	0.240	20m 01s	767 MB
Half cosine (7K)	0.737	25.46	0.316	2m 52s	400 MB	0.749	21.07	0.295	1m 42s	244 MB	0.872	27.938	0.320	2m 42s	355 MB
Half cosine (30K)	0.790	27.04	0.247	16m 15s	524 MB	0.824	23.11	0.201	9m 11s	338 MB	0.900	29.38	0.253	17m 35s	634 MB
Modular Sinc (7K)	0.751	25.74	0.302	3m 20s	439 MB	0.767	21.59	0.276	2m 04s	255 MB	0.878	28.39	0.308	3m 17s	399 MB
Modular Sinc (30K)	0.801	27.30	0.234	18m 50s	622 MB	0.836	23.51	0.189	16m 08s	333 MB	0.901	29.66	0.247	20m 47s	682 MB
Parabola (7K)	0.7460	25.63	0.3080	3m 8s	423 MB	0.7602	21.33	0.2818	1m 48s	241 MB	0.8773	28.26	0.3126	2m 51s	347 MB
Parabola (30K)	0.7971	27.15	0.2399	17m 23s	542 MB	0.831	23.28	0.1935	10m 24s	317 MB	0.902	29.53	0.2489	18m 57s	516 MB
Inverse MQ (7K)	0.7443	25.25	0.3008	3m 19s	281 MB	0.76	21.365	0.2765	2m 6s	175 MB	0.874	28.09	0.3095	3m 10s	248 MB
Inverse MQ (30K)	0.7932	26.82	0.2258	16m	365 MB	0.8305	23.343	0.1875	10m 13s	223.5 MB	0.9005	29.504	0.2435	18m 10s	364 MB

Table 3. **Splatting results.** The best values are highlighted in red and second-best values in orange and the third-best values in yellow. Note that, * denotes the difference in computation power that is used to implement our model and previous models (3DGS [11], GES [10]), hence we used a speed-up factor (*see Supplementary Materials*), to obtain fair results compared to the training time in the original publications. Our DARBFs were implemented based on the *updated* 3DGS codebase. Notice, half-cosine shows a significant reduction in training time, while inverse multiquadric shows a significant reduction in memory footprint. Additionally, the raised cosine kernel achieves modest gains in PSNR, SSIM, LPIPS and training duration. We evaluate the performance of each model by considering the results at 7K and 30K iteration checkpoints (here, Inverse MQ means inverse multiquadric function and Parabola means $1 - \frac{1}{9}(d_M)^2$).

Material). Meanwhile, half-cosines, modular sines, and parabolic functions achieve on-par PSNR, SSSIM, LPIPS results. This also demonstrates that certain DARBFs, despite not belonging to the exponential family, can compete effectively with previous benchmarked work [10].

Reduced memory footprint. Table 3 shows that the inverse multiquadric (Inverse MQ) function reduces memory usage by over a significant 45%, while half-cosines achieve a 14% reduction on average compared to Gaussians. Fig. 5 illustrates this with 1D plots of half-cosine ($\beta = 2$ for modified half-cosine in Table 1), Gaussians, and Inverse MQ. A single primitive with the same variance spans a larger region with higher opacity in cosine and Inverse MQ functions, reducing the need for multiple splats to achieve the same accumulated value. This is further illustrated by the visual comparison of artifact shapes in the Gaussian and half-cosine reconstructed scenes shown in Fig. 6. A similar conclusion applies to Inverse MQ.

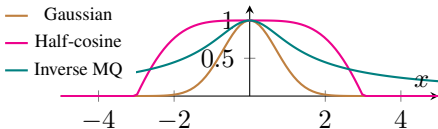


Figure 5. Comparison of various reconstruction kernels with the same variance, using parameters as specified in Table 2. Notice the blunt peak in the half-cosine curve, the wide-spread area under the inverse MQ curve, and the sharp peak in the Gaussian curve, all of which contribute to their differing performances.

Training efficiency. Table 3 shows that half-cosines ($\xi = \frac{18}{\pi}$) achieve a 15% reduction in training time on average compared to Gaussians (*updated codebase*) and 12-34% speedups across different scenes. Although cosine computations are more computationally intensive than Gaussians, this improvement stems from the pre-computed scalar correction factor, lower primitive count, and steeper roll-off in half-cosines. The training loss and speed plots, (*see Supplementary Materials*) further demonstrate this by comparing across DARBFs. Despite similar training loss curves to 3DGS, half-cosine splatting outperforms Gaussians in terms of training speed. This can be attributed to half-cosines leveraging fewer, higher-span primitives with a steeper roll-off (Fig. 5), which enhances gradient updates and enables faster convergence. Additionally, do note that this training efficiency is irrespective of hardware performance (*see Supplementary Materials*).

Convergence experiments. We acknowledge that the objective function remains Lipschitz continuous, with smoothness varying across reconstruction kernels. Table 4 shows that neither kernel performs optimally at extreme learning rates, and while cosine kernels induce less smoothness than Gaussians, their steeper roll-off and sparse gradients enable faster convergence at optimal rates. As this is the first study exploring the behavior of non-exponential kernels in this context, what we established here, that DARBFs can successfully replace Gaussians in 3DGS, is, in our opinion, significant. We defer a detailed mathematical analysis on convergence to future work.



(a) The famous blurred, blunt-peaked artifacts of Gaussians due to its sharp peak.

(b) Round-shaped artifacts of half-cosines due to its lengthy blunt peak.

Figure 6. Comparison of rendered views between different DARBFs from the Garden scene (Mip-NeRF 360 dataset). This aligns with the inherent shape of half-cosines due to its lengthy blunt peak as graphically modeled in Fig. 1 & 5, helps reduce artifacts caused by the needle-shaped Gaussians in certain cases.

LR	PSNR		Training Time		Memory	
	Gaussian	HC	Gaussian	HC	Gaussian	HC
0.01	31.49	31.34	22m 31s	23m 26s	255.61 MB	246.48 MB
0.02	31.75	31.34	19m 48s	17m 32s	293.61 MB	282.65 MB
0.1	31.1	29.38	13m 31s	11m 20s	364 MB	391.76 MB
0.2	30.5	26.54	10m 34s	8m 26s	241.42 MB	315.93 MB

Table 4. Comparison of Gaussian and half-cosine (HC) methods based on PSNR, Training Time, and Memory usage for different learning rates.

These experiments show that users can select sharp-peaked kernels (Gaussians, raised-cosines) for detailed scenes to ensure finer reconstruction, whereas for large-scale scenes with memory and inference constraints, blunt-peaked widely-spanned kernels like half-cosines and inverse multiquadrics are preferable.

5.2. Ablations

Choosing Decay in ARBFs. We validated various reconstruction kernels through low-dimensional simulations (Fig. 3), showing that normalized, decaying functions focus energy near the origin (Sec. 4.1), ensuring each sample’s influence on the reconstruction is strongest its point, aiding accurate signal reconstruction. In contrast, the instability caused by unbounded growing functions led to their omission in favor of DARBFs.

Correction factor. As discussed in (Sec. 4.1), we introduce ψ , a novel correction factor, to approximate the closure property of Gaussians. We evaluated three cases (Table 5): (1) without ψ , (2) with matrix ψ from an MLP, and (3) with scalar ψ precomputed from closed-form regression experiments (scalar ψ is more computationally efficient, hence we select it).

Table 6 shows that these modifications significantly improved DARBF performance, achieving comparable results to the *updated* 3DGS codebase on the Mip-NeRF 360 [12]

dataset.

Method	SSIM \uparrow	PSNR \uparrow	LPIPS \downarrow
Gaussian w/o ψ	0.81	27.45	0.22
HC w/o ψ	0.76	25.89	0.28
HC w/ ψ (MLP)	0.794	27.17	0.24
HC w/ ψ (Scalar)	0.795	27.16	0.238

Table 5. Performance comparison of different types of correction factors (ψ) on Gaussian and half-cosine (HC) kernels across selected scenes from the Mip-NeRF 360 dataset. The results show that the scalar correction factor approximation from precomputed closed-form regression achieves comparable results to the MLP-derived correction factor. Additionally, observe how HC without ψ underperforms the same with ψ .

Scenes	with ψ			without ψ		
	PSNR	SSIM	LPIPS	PSNR	SSIM	LPIPS
3DGS-updated	—	—	—	27.45	0.81	0.22
Raised Cosine	27.45	0.81	0.21	26.69	0.78	0.25
Half Cosine	27.04	0.79	0.25	25.89	0.76	0.28

Table 6. Comparison of PSNR, SSIM, and LPIPS metrics for Mip-NeRF 360 scenes with ψ , showing that its incorporation enhances kernel performance and is useful to producing comparable results to 3DGS.

6. Conclusion

To the best of our knowledge, we are the first to generalize splatting techniques with DARB-Splatting, extending beyond the conventional exponential family. In introducing this new class of functions, DARBFs, we highlight the distinct performances of each function. We establish the relationships between 3D covariance and 2D projected covariance, providing an effective approach for understanding covariance transformations under projection. Our modified CUDA codes for each DARBF are available to facilitate further research and exploration in this area.

Limitation. While we push the boundaries of splatting functions with DARBFs, the useful properties and capabilities of each function for 3D reconstruction, within a classified mathematical framework, remain to be fully explored. Future research could explore utility applications and the incorporation of existing signal reconstruction algorithms, such as the Gram-Schmidt process, with DARBFs.

7. Acknowledgments

The authors acknowledge the University of Moratuwa for conference publication support. They also thank the University of Moratuwa Alumni Batch ’96 and the Accelerating Higher Education Expansion and Development (AHEAD) Operation of the Ministry of Higher Education, Sri Lanka, funded by the World Bank, for generous computational resources.

References

- [1] Jonathan T. Barron, Ben Mildenhall, Matthew Tancik, Peter Hedman, Ricardo Martin-Brualla, and Pratul P. Srinivasan. Mip-nerf: A multiscale representation for anti-aliasing neural radiance fields. In *ICCV*, pages 5835–5844, 2021. 2
- [2] Jonathan T Barron, Ben Mildenhall, Dor Verbin, Pratul P Srinivasan, and Peter Hedman. Zip-nerf: Anti-aliased grid-based neural radiance fields. In *CVPR*, pages 19697–19705, 2023. 2
- [3] Christopher M Bishop and Nasser M Nasrabadi. *Pattern recognition and machine learning*. Springer, 2006. 4
- [4] R.L. Burden and J.D. Faires. *Numerical Analysis*. Cengage Learning, 2010. 5
- [5] G. Casciola, D. Lazzaro, L.B. Montefusco, and S. Morigi. Shape preserving surface reconstruction using locally anisotropic radial basis function interpolants. *Computers & Mathematics with Applications*, 51(8):1185–1198, 2006. Radial Basis Functions and Related Multivariate Meshfree Approximation Methods: Theory and Applications. 3, 12
- [6] Yiwen Chen, Zilong Chen, Chi Zhang, Feng Wang, Xiaofeng Yang, Yikai Wang, Zhongang Cai, Lei Yang, Huaping Liu, and Guosheng Lin. Gaussianeditor: Swift and controllable 3d editing with gaussian splatting. In *CVPR*, pages 21476–21485, 2024. 2
- [7] Yuedong Chen, Haofei Xu, Chuanxia Zheng, Bohan Zhuang, Marc Pollefeys, Andreas Geiger, Tat-Jen Cham, and Jianfei Cai. Mvsplat: Efficient 3D gaussian splatting from sparse multi-view images. In *ECCV*, pages 370–386, 2025. 2
- [8] Jaeyoung Chung, Suyoung Lee, Hyeongjin Nam, Jaerin Lee, and Kyoung Mu Lee. Luciddreamer: Domain-free generation of 3d gaussian splatting scenes, 2023. 2
- [9] Kangle Deng, Andrew Liu, Jun-Yan Zhu, and Deva Ramanan. Depth-supervised nerf: Fewer views and faster training for free. In *CVPR*, pages 12882–12891, 2022. 2
- [10] A. Hamdi et al. Ges: Generalized exponential splatting for efficient radiance field rendering. *CVPR*, 2024. 2, 3, 6, 7, 19, 20, 21
- [11] B. Kerbl et al. 3d gaussian splatting for real-time radiance field rendering. *ACM TOG*, 42(4), July 2023. 1, 2, 3, 5, 6, 7, 12, 13, 14, 19, 20, 21
- [12] J. T. Barron et al. Mip-nerf 360: Unbounded anti-aliased neural radiance fields. In *CVPR*, pages 5470–5479, 2022. 2, 6, 8, 19, 21, 31
- [13] Ben Fei, Jingyi Xu, Rui Zhang, Qingyuan Zhou, Weidong Yang, and Ying He. 3d gaussian splatting as new era: A survey. *IEEE Transactions on Visualization and Computer Graphics*, 2024. 2
- [14] Sara Fridovich-Keil, Alex Yu, Matthew Tancik, Qinhong Chen, Benjamin Recht, and Angjoo Kanazawa. Plenoxels: Radiance fields without neural networks. In *CVPR*, pages 5501–5510, 2022. 21
- [15] Stephan J Garbin, Marek Kowalski, Matthew Johnson, Jamie Shotton, and Julien Valentin. Fastnerf: High-fidelity neural rendering at 200fps. In *ICCV*, pages 14346–14355, 2021. 2
- [16] Yuanhao Gong. Eggs: Edge guided gaussian splatting for radiance fields, 2024. 2
- [17] Steven J. Gortler, Radek Grzeszczuk, Richard Szeliski, and Michael F. Cohen. The lumigraph. In *Proceedings of the 23rd Annual Conference on Computer Graphics and Interactive Techniques, SIGGRAPH '96*, page 43–54, New York, NY, USA, 1996. Association for Computing Machinery. 2
- [18] Ayaan Haque, Matthew Tancik, Alexei A Efros, Aleksander Holynski, and Angjoo Kanazawa. Instruct-nerf2nerf: Editing 3d scenes with instructions. In *CVPR*, pages 19740–19750, 2023. 2
- [19] Peter Hedman, Julien Philip, True Price, Jan-Michael Frahm, George Drettakis, and Gabriel Brostow. Deep blending for free-viewpoint image-based rendering. *ACM Transactions on Graphics (Proc. SIGGRAPH Asia)*, 37(6):257:1–257:15, 2018. 6, 19, 32
- [20] Jan Held, Renaud Vandeghen, Adrien Deliege, Abdullah Hamdi, Anthony Cioppa, Silvio Giancola, Andrea Vedaldi, Bernard Ghanem, Andrea Tagliasacchi, and Marc Van Droogenbroeck. Triangle splatting for real-time radiance field rendering. *arXiv*, 2025. 3
- [21] Jan Held, Renaud Vandeghen, Abdullah Hamdi, Adrien Deliege, Anthony Cioppa, Silvio Giancola, Andrea Vedaldi, Bernard Ghanem, and Marc Van Droogenbroeck. 3d convex splatting: Radiance field rendering with 3d smooth convexes. In *Proceedings of the IEEE/CVF Conference on Computer Vision and Pattern Recognition (CVPR)*, 2025. 3
- [22] Tongyan Hua and Lin Wang. Benchmarking implicit neural representation and geometric rendering in real-time rgb-d slam. In *CVPR*, pages 21346–21356, June 2024. 2
- [23] Jiajun Huang, Hongchuan Yu, Jianjun Zhang, and Hammadi Nait-Charif. Point'n move: Interactive scene object manipulation on gaussian splatting radiance fields. *IET Image Processing*, 2024. 2
- [24] Junha Hyung, Susung Hong, Sungwon Hwang, Jaeseong Lee, Jaegul Choo, and Jin-Hwa Kim. Effective rank analysis and regularization for enhanced 3d gaussian splatting. *arXiv preprint arXiv:2406.11672*, 2024. 2
- [25] Muhammad Osama Khan and Yi Fang. Implicit neural representations for medical imaging segmentation. In *Medical Image Computing and Computer Assisted Intervention – MICCAI 2022*, pages 433–443, 2022. 2
- [26] Arno Knapitsch, Jaesik Park, Qian-Yi Zhou, and Vladlen Koltun. Tanks and temples: Benchmarking large-scale scene reconstruction. *ACM Transactions on Graphics*, 36(4), 2017. 6, 19, 32
- [27] Agelos Kratimenos, Jiahui Lei, and Kostas Daniilidis. Dynmf: Neural motion factorization for real-time dynamic view synthesis with 3d gaussian splatting. In *ECCV*, pages 252–269. Springer, 2025. 2
- [28] Lambda Labs. GPU Benchmarks, 2024. Accessed: Nov. 20, 2024. 19
- [29] Christoph Lassner and Michael Zollhöfer. Pulsar: Efficient sphere-based neural rendering. In *CVPR*, June 2021. 4
- [30] Joo Chan Lee, Daniel Rho, Xiangyu Sun, Jong Hwan Ko, and Eunbyung Park. Compact 3d gaussian representation for radiance field. In *CVPR*, pages 21719–21728, 2024. 2
- [31] Stanford Lee, Dario Macagnano, and Eric Cornwell. 3d gaussian splatting: Performant 3d scene reconstruction at scale. <https://aws.amazon.com/>

[blogs / spatial / 3d-gaussian-splatting-performant-3d-scene-reconstruction-at-scale/](#), 2024. Accessed: 2025-03-07. 1

- [32] Jiahui Lei, Yufu Wang, Georgios Pavlakos, Lingjie Liu, and Kostas Daniilidis. Gart: Gaussian articulated template models. In *CVPR*, pages 19876–19887, 2024. 2
- [33] Marc Levoy and Pat Hanrahan. Light field rendering. In *Proceedings of the 23rd Annual Conference on Computer Graphics and Interactive Techniques, SIGGRAPH '96*, page 31–42, New York, NY, USA, 1996. Association for Computing Machinery. 2
- [34] Haolin Li, Jinyang Liu, Mario Sznaiar, and Octavia Camps. 3d-hgs: 3d half-gaussian splatting. *arXiv preprint arXiv:2406.02720*, 2024. 2, 3
- [35] David B Lindell, Julien NP Martel, and Gordon Wetzstein. Autoint: Automatic integration for fast neural volume rendering. In *CVPR*, pages 14556–14565, 2021. 2
- [36] Lingjie Liu, Jiatao Gu, Kyaw Zaw Lin, Tat-Seng Chua, and Christian Theobalt. Neural sparse voxel fields. pages 15651–15663, 2020. 2
- [37] Steven Liu, Xiuming Zhang, Zhoutong Zhang, Richard Zhang, Jun-Yan Zhu, and Bryan Russell. Editing conditional radiance fields. In *CVPR*, pages 5773–5783, 2021. 2
- [38] Ricardo Martin-Brualla, Noha Radwan, Mehdi S. M. Sajjadi, Jonathan T. Barron, Alexey Dosovitskiy, and Daniel Duckworth. Nerf in the wild: Neural radiance fields for unconstrained photo collections. In *CVPR*, pages 7210–7219, June 2021. 2
- [39] Ben Mildenhall, Peter Hedman, Ricardo Martin-Brualla, Pratul P Srinivasan, and Jonathan T Barron. Nerf in the dark: High dynamic range view synthesis from noisy raw images. In *CVPR*, pages 16190–16199, 2022. 2
- [40] Ben Mildenhall, Pratul P. Srinivasan, Matthew Tancik, Jonathan T. Barron, Ravi Ramamoorthi, and Ren Ng. NeRF: Representing scenes as neural radiance fields for view synthesis. In *ECCV*, 2020. 2
- [41] Thomas Müller, Alex Evans, Christoph Schied, and Alexander Keller. Instant neural graphics primitives with a multiresolution hash encoding. *ACM TOG*, 41(4):1–15, 2022. 21
- [42] KL Navaneet, Kossar Pourahmadi Meibodi, Soroush Abbasi Koohpayegani, and Hamed Pirsiavash. Compgs: Smaller and faster gaussian splatting with vector quantization. *ECCV*, 2024. 2, 3
- [43] Simon Niedermayr, Josef Stumpfegger, and Rüdiger Westermann. Compressed 3d gaussian splatting for accelerated novel view synthesis. In *Proceedings of the IEEE/CVF Conference on Computer Vision and Pattern Recognition (CVPR)*, pages 10349–10358, June 2024. 3
- [44] Panagiotis Papantonakis, Georgios Kopanas, Bernhard Kerbl, Alexandre Lanvin, and George Drettakis. Reducing the memory footprint of 3d gaussian splatting. *Proc. ACM Comput. Graph. Interact. Tech.*, 7(1), May 2024. 3
- [45] Keunhong Park, Utkarsh Sinha, Jonathan T Barron, Sofien Bouaziz, Dan B Goldman, Steven M Seitz, and Ricardo Martin-Brualla. Nerfies: Deformable neural radiance fields. In *CVPR*, pages 5865–5874, 2021. 2
- [46] Keunhong Park, Utkarsh Sinha, Peter Hedman, Jonathan T Barron, Sofien Bouaziz, Dan B Goldman, Ricardo Martin-Brualla, and Steven M Seitz. Hypernerf: A higher-dimensional representation for topologically varying neural radiance fields. *arXiv preprint arXiv:2106.13228*, 2021. 2
- [47] Albert Pumarola, Enric Corona, Gerard Pons-Moll, and Francesc Moreno-Noguer. D-nerf: Neural radiance fields for dynamic scenes. In *CVPR*, pages 10318–10327, 2021. 2
- [48] Shiyu Qiu, Chunlei Wu, Zhenghao Wan, and Siyuan Tong. High-fold 3d gaussian splatting model pruning method assisted by opacity. *Applied Sciences*, 15, 2025. 2
- [49] Daniel Rebain, Wei Jiang, Soroosh Yazdani, Ke Li, Kwang Moo Yi, and Andrea Tagliasacchi. Derf: Decomposed radiance fields. In *CVPR*, pages 14153–14161, 2021. 2
- [50] Christian Reiser, Songyou Peng, Yiyi Liao, and Andreas Geiger. Kilonerf: Speeding up neural radiance fields with thousands of tiny mlps. In *CVPR*, pages 14335–14345, 2021. 2
- [51] Jiawei Ren, Liang Pan, Jiaxiang Tang, Chi Zhang, Ang Cao, Gang Zeng, and Ziwei Liu. Dreamgaussian4d: Generative 4d gaussian splatting, 2024. 2
- [52] Barbara Roessle, Jonathan T Barron, Ben Mildenhall, Pratul P Srinivasan, and Matthias Nießner. Dense depth priors for neural radiance fields from sparse input views. In *CVPR*, pages 12892–12901, 2022. 2
- [53] Hemanth Saratchandran, Sameera Ramasinghe, Violetta Shevchenko, Alexander Long, and Simon Lucey. A sampling theory perspective on activations for implicit neural representations, 2024. 2
- [54] Johannes L Schonberger and Jan-Michael Frahm. Structure-from-motion revisited. In *CVPR*, pages 4104–4113, 2016. 2, 3, 6
- [55] Katja Schwarz, Yiyi Liao, Michael Niemeyer, and Andreas Geiger. Graf: Generative radiance fields for 3d-aware image synthesis. In *NeurIPS*, pages 20154–20166, 2020. 2
- [56] Ruizhi Shao, Jingxiang Sun, Cheng Peng, Zerong Zheng, Boyao Zhou, Hongwen Zhang, and Yebin Liu. Control4d: Dynamic portrait editing by learning 4d gan from 2d diffusion-based editor. *arXiv preprint arXiv:2305.20082*, 2(6):16, 2023. 2
- [57] Jin-Chuan Shi, Miao Wang, Hao-Bin Duan, and Shao-Hua Guan. Language embedded 3d gaussians for open-vocabulary scene understanding, 2023. 2
- [58] A. Skodras, C. Christopoulos, and T. Ebrahimi. The jpeg 2000 still image compression standard. *IEEE Signal Processing Magazine*, 18(5):36–58, 2001. 2
- [59] Noah Snavely, Steven M. Seitz, and Richard Szeliski. Photo tourism: exploring photo collections in 3d. *ACM Trans. Graph.*, 25(3):835–846, July 2006. 2, 3
- [60] Kun Su, Mingfei Chen, and Eli Shlizerman. Inras: Implicit neural representation for audio scenes. In *NeurIPS*, pages 8144–8158, 2022. 2
- [61] Cheng Sun, Jaesung Choe, Charles Loop, Wei-Chiu Ma, and Yu-Chiang Frank Wang. Sparse voxels rasterization: Real-time high-fidelity radiance field rendering. In *CVPR*, 2025. 3

- [62] Jiakai Sun, Han Jiao, Guangyuan Li, Zhanjie Zhang, Lei Zhao, and Wei Xing. 3dstream: On-the-fly training of 3d gaussians for efficient streaming of photo-realistic free-viewpoint videos. In *CVPR*, pages 20675–20685, 2024. [2](#)
- [63] Jingxiang Sun, Xuan Wang, Yong Zhang, Xiaoyu Li, Qi Zhang, Yebin Liu, and Jue Wang. Fenerf: Face editing in neural radiance fields. In *CVPR*, pages 7672–7682, 2022. [2](#)
- [64] Matthew Tancik, Vincent Casser, Xinchun Yan, Sabeek Pradhan, Ben Mildenhall, Pratul P Srinivasan, Jonathan T Barron, and Henrik Kretzschmar. Block-nerf: Scalable large scene neural view synthesis. In *CVPR*, pages 8248–8258, 2022. [2](#)
- [65] Jiaxiang Tang, Jiawei Ren, Hang Zhou, Ziwei Liu, and Gang Zeng. Dreamgaussian: Generative gaussian splatting for efficient 3d content creation, 2024. [2](#)
- [66] G.K. Wallace. The jpeg still picture compression standard. *IEEE Transactions on Consumer Electronics*, 38(1):xviii–xxxiv, 1992. [2](#)
- [67] Lee Westover. Interactive volume rendering. In *Proceedings of the 1989 Chapel Hill Workshop on Volume Visualization*, VVS '89, page 9–16, New York, NY, USA, 1989. Association for Computing Machinery. [2](#), [3](#)
- [68] Lee Westover. Footprint evaluation for volume rendering. In *Proceedings of the 17th Annual Conference on Computer Graphics and Interactive Techniques*, SIGGRAPH '90, page 367–376, New York, NY, USA, 1990. Association for Computing Machinery. [3](#)
- [69] Guanjun Wu, Taoran Yi, Jiemin Fang, Lingxi Xie, Xiaopeng Zhang, Wei Wei, Wenyu Liu, Qi Tian, and Xinggang Wang. 4d gaussian splatting for real-time dynamic scene rendering. In *CVPR*, pages 20310–20320, 2024. [2](#)
- [70] Tianyi Xie, Zeshun Zong, Yuxing Qiu, Xuan Li, Yutao Feng, Yin Yang, and Chenfanfu Jiang. Physgaussian: Physics-integrated 3d gaussians for generative dynamics. In *CVPR*, pages 4389–4398, 2024. [2](#)
- [71] Chi Yan, Delin Qu, Dan Xu, Bin Zhao, Zhigang Wang, Dong Wang, and Xuelong Li. Gs-slam: Dense visual slam with 3d gaussian splatting. In *CVPR*, pages 19595–19604, 2024. [2](#)
- [72] Bangbang Yang, Yinda Zhang, Yinghao Xu, Yijin Li, Han Zhou, Hujun Bao, Guofeng Zhang, and Zhaopeng Cui. Learning object-compositional neural radiance field for editable scene rendering. In *CVPR*, pages 13779–13788, 2021. [2](#)
- [73] Mingqiao Ye, Martin Danelljan, Fisher Yu, and Lei Ke. Gaussian grouping: Segment and edit anything in 3d scenes. In *ECCV*, 2024. [2](#)
- [74] Vickie Ye and Angjoo Kanazawa. Mathematical supplement for the `gsplat` library, 2023. [4](#), [6](#)
- [75] Taoran Yi, Jiemin Fang, Junjie Wang, Guanjun Wu, Lingxi Xie, Xiaopeng Zhang, Wenyu Liu, Qi Tian, and Xinggang Wang. Gaussiandreamer: Fast generation from text to 3d gaussians by bridging 2D and 3D diffusion models. In *CVPR*, pages 6796–6807, 2024. [2](#)
- [76] Heng Yu, Joel Julin, Zoltán A. Milacski, Koichiro Niinuma, and László A. Jeni. Cogs: Controllable gaussian splatting. In *CVPR*, pages 21624–21633, June 2024. [2](#)
- [77] Ruihan Yu, Tianyu Huang, Jingwang Ling, and Feng Xu. 2dgh: 2d gaussian-hermite splatting for high-quality rendering and better geometry reconstruction. *arXiv preprint arXiv:2408.16982*, 2024. [2](#), [3](#)
- [78] Zehao Yu, Anpei Chen, Binbin Huang, Torsten Sattler, and Andreas Geiger. Mip-splatting: Alias-free 3D Gaussian splatting. In *CVPR*, pages 19447–19456, June 2024. [2](#)
- [79] Zehao Yu, Anpei Chen, Binbin Huang, Torsten Sattler, and Andreas Geiger. Mip-splatting: Alias-free 3d gaussian splatting. In *CVPR*, pages 19447–19456, 2024. [2](#)
- [80] Jiahui Zhang, Fangneng Zhan, Muyu Xu, Shijian Lu, and Eric Xing. Fregs: 3d gaussian splatting with progressive frequency regularization. *arXiv preprint arXiv:2403.06908*, 2024. [2](#)
- [81] Fuqiang Zhao, Wei Yang, Jiakai Zhang, Pei Lin, Yingliang Zhang, Jingyi Yu, and Lan Xu. Humannerf: Efficiently generated human radiance field from sparse inputs. In *CVPR*, pages 7743–7753, 2022. [2](#)
- [82] Matthias Zwicker, Hanspeter Pfister, Jeroen van Baar, and Markus Gross. Ewa splatting. *IEEE Transactions on Visualization and Computer Graphics*, 8(3):223–238, July 2002. [2](#), [3](#), [4](#), [5](#), [12](#), [13](#), [20](#)

DARB-Splatting: Generalizing Splatting with Decaying Anisotropic Radial Basis Functions

Supplementary Material

A. DARB-Splatting

We generalize the reconstruction kernel to include non-exponential functions by introducing a broader class of Decaying Anisotropic Radial Basis Functions (DARBFs). One of the main reasons why non-exponential functions have not been widely explored is the advantageous integration property of the Gaussian function, which simplifies the computation of the 2D covariance of a splat. However, through Monte Carlo experiments, we demonstrate that DARBFs can also exhibit this desirable property, even though most of them lack a closed-form solution for integration. Additionally, the integration of DARBFs does not generally relate to other DARBFs.

We also explained (Sec. 4.1), using an example, that in 3DGS [11], the opacity contribution for each pixel from a reconstruction kernel (3D) is derived from its splats (2D), rather than from their 3D volume. Based on this, we consider the covariance in 3D as a variable representing the 2D covariances in all directions. In the next section, we describe the Monte Carlo experiments we conducted, supported by mathematical equations.

In surface reconstruction tasks [5], DARBFs leverage principal component analysis (PCA) of the local covariance matrix to identify directionally dependent features and orient the 3D ellipsoids accordingly. This approach enables DARBFs to model local anisotropies in the data and reconstruct surfaces, preserving fine details more effectively than isotropic models. Furthermore, the decaying nature of these functions, as presented in Table 1, results in a more localized influence, effectively focusing the function within a certain radius. This localization is advantageous in 3D reconstruction, where only neighboring points contribute significantly to a given point in space, ensuring smooth blending. Therefore, we can conclude that all DARBFs are suitable for splatting. Although there are many DARBFs, we focus on a selected few here due to limited space. In the following sections, we elaborate on the mathematical formulation of these selected DARBFs, outline their computational implementation, and demonstrate their utility in accurately modeling complex opacity distributions in the context of 3D scene reconstruction.

A.1. Assessing DARBFs in Simulations

Motivation. We evaluate and compare the performance of our DARB reconstruction kernels against conventional Gaussian kernels through simulations in lower-dimensional settings. We generated various synthetic 1D functions

across a specified range, including *square*, *exponential*, *truncated-sinusoid*, *Gaussian*, and *triangular pulses*, as well as some irregular functions to simulate real-world signal variability. These signals were reconstructed using Gaussian functions and various DARBFs to evaluate the number of primitives required for accurate reconstruction and the cost difference between original and reconstructed signals.

This pipeline optimizes the number of primitives needed for signal approximation across different reconstruction kernels. Our approach focuses on three key parameters: position, covariance (for signal spread), and amplitude (for signal strength). The model configurations comprises a mixture network of *Gaussian*, *half-cosine*, *raised-cosine*, and *modular sinc* components, each with a predefined variable number of components.

Training Recipe. The model was trained for a fixed number of epochs with respect to a mean squared error loss function, which minimized reconstruction error between the predicted and target signals. Unlike the original Gaussian Splatting algorithm [11], which calculates loss in the projected 2D image space with reconstruction in 3D space, we simplified by calculating the loss and performing the reconstruction directly in 1D because, 1D signal projection cannot be represented in 0D, as this would be meaningless. Finally, a parameter sweep was conducted to identify the optimal configuration with the lowest recorded loss, indicating the optimal number of components. We provide an extensive experimental analysis of 1D simulations in Sec. D.

A.2. Mathematical Expressions of Monte Carlo Experiments

When it comes to 3DGS [11], we initially start with a 3×3 covariance matrix in the 3D world coordinate system. By using,

$$\Sigma' = JW\Sigma W^T J^T \quad (12)$$

we obtain a 3×3 covariance matrix (Σ') in the camera coordinate space. According to the integration property mentioned in the EWA Splatting paper [82], this Σ' can be projected into a 2×2 covariance matrix in the image space ($\Sigma'_{2 \times 2}$) by simply removing the third row and column of Σ' . However, the same process does not apply to other DARBFs. For instance, there is no closed-form solution for the marginal integration of the half-cosine and raised-cosine functions used in this paper. To simplify the understanding

of this integration process and address this issue, we conducted the following experiment.

Experimental Setup. First, we introduce our 3D point space with x, y, z coordinates in equally spaced intervals for N number of points, a random mean vector (μ) and a random 3×3 covariance matrix (Σ). Based on a predetermined limit specific for each DARBF (we will discuss about this in Sec. A.3), we calculate the density/power assigned by the DARB kernel at a particular point \mathbf{x} in 3D space as follows:

$$P = \cos \left(\frac{2\pi (\mathbf{x} - \boldsymbol{\mu})^T (\Sigma)^{-1} (\mathbf{x} - \boldsymbol{\mu})}{36} \right), \quad (13)$$

where $\mathbf{x} = [x_i \ y_i \ z_i]$. As for the integration, we take the sum of these P ($P \in \mathbb{R}^{N \times N \times N}$) matrices along one dimension (for instance, along z axis) and name it *total_density*, which can be obtained as follows:

$$\text{total_density}(x, y) = \sum_z P(x, y, z) \quad (14)$$

where *total_density* $\in \mathbb{R}^{N \times N}$. This will, for example, integrate the cosine kernel in Eq. 13 along z -direction, collapsing into a 2D density in XY plane. Following this integration, these total densities will be normalized as follows:

$$\text{total_density}_{\text{normalized}} = \frac{\text{total_density}}{\max(\text{total_density})} \quad (15)$$

This normalization step does not change the typical covariance relationship. To compare with other functions' projection better, we use this normalization, so that the maximum of total density will be equal one.

For the visualization of these 2D densities, we create a 2D mesh grid by using only x, y coordinate matrices called *coords* $\in \mathbb{R}^{N^2 \times 2}$. At the same time, we flatten the 2D density matrix and get a density grid as *density* $\in \mathbb{R}^{N^2 \times 1}$.

If the dimensions of x, y coordinates are different, we need to repeat the *coords* and *density* arrays separately to perfectly align each 2D coordinate for its corresponding density value. Since we use the same dimension for x, y coordinates, we can skip this step. By using these *coords* and *density* matrices, we then calculate the weighted covariance matrix as follows:

$$\bar{x} = \frac{\sum_{i=1}^{N'} w_i x_i}{\sum_{i=1}^{N'} w_i} \quad \bar{y} = \frac{\sum_{i=1}^{N'} w_i y_i}{\sum_{i=1}^{N'} w_i}$$

where $N' = N^2$ and w_i denote the corresponding parameters from the *density* matrix. Finally, the vector $\bar{\mathbf{m}}$ is given by:

$$\bar{\mathbf{m}} = \begin{bmatrix} \bar{x} \\ \bar{y} \end{bmatrix}_{2 \times 1} \quad (16)$$

By using the above results, we can determine the projected 2×2 covariance matrix ($\Sigma'_{2 \times 2}$) as follows:

$$\Sigma'_{2 \times 2} = \begin{bmatrix} \sigma_{xx} & \sigma_{xy} \\ \sigma_{xy} & \sigma_{yy} \end{bmatrix}$$

where σ_{xx} , σ_{yy} and σ_{xy} terms can be determined as:

$$\sigma_{xx} = \frac{\sum_{i=1}^N w_i (x_i - \bar{x})^2}{\sum_{i=1}^N w_i} \quad \sigma_{yy} = \frac{\sum_{i=1}^N w_i (y_i - \bar{y})^2}{\sum_{i=1}^N w_i}$$

$$\sigma_{xy} = \frac{\sum_{i=1}^N w_i (x_i - \bar{x})(y_i - \bar{y})}{\sum_{i=1}^N w_i}$$

We can express this entire operation in matrix form as follows:

$$\Sigma'_{2 \times 2} = \frac{1}{\sum_{i=1}^{N'} w_i} \sum_{i=1}^{N'} w_i (\mathbf{x}_i - \bar{\mathbf{m}}) (\mathbf{x}_i - \bar{\mathbf{m}})^T \quad (17)$$

$$\text{where } \mathbf{x}_i = \begin{bmatrix} x_i \\ y_i \end{bmatrix}$$

Based on this simulation, we received the projected 2×2 covariance matrix ($\Sigma'_{2 \times 2}$) for different DARBFs and identified that they are not integrable for volume rendering [82]. Simply saying, we cannot directly obtain the first two rows and columns of $\Sigma'_{2 \times 2}$ from the first two rows and first two columns of the 3D covariance matrix $\Sigma'_{3 \times 3}$ as they are. **Correction Factor (ψ).** Since most of the DARB functions do not have closed form integration,

But we noticed that there is a common ratio between the values of these two matrices. To resolve this issue, we introduce a correction factor ψ as a scalar to multiply with the $\Sigma'_{2 \times 2}$ matrix. This scalar holds different values for different DARBFs since their density kernels act differently.

A.3. Determining the Boundaries of DARBFs

From the 1D signal reconstruction simulations (Sec. A.1 and Sec. D) and the splatting results (Sec. D), we demonstrate that strictly decaying functions can represent the scenes better. Therefore, we use the limits for each function to ensure the strictly decaying nature, while also considering the size of each splat. By restricting to a single pulse, we achieve a more localized representation, resulting in better quality. Incorporating more pulses allows them to cover a larger region compared to one pulse (with the same ξ and β), leading to memory reduction, albeit with a tradeoff in quality.

In 3DGS [11], opacity modeling happens after the projection of the 3D covariance (Σ) in world coordinate space onto 2D covariance ($\Sigma'_{2 \times 2}$) in image space. By using the inverse covariance ($\Sigma'^{-1}_{2 \times 2}$) and the difference between the center of the splat (μ') and the coordinates of the selected pixel, they introduce the Mahalanobis component (Eq. 1) within the Gaussian kernel to model the opacity distribution across each splat. When determining the final color of a particular pixel, they have incorporated a bounding box mechanism to identify the area which a splat can have the effect when modeling the opacity, so that they can do the

tile-based rasterization using the computational resources efficiently.

Since the Gaussian only has a main lobe, we can simply model the opacity distribution across a splat using the bounding box mentioned in Sec. 4.1. This bounding box, determined by the radius $R = 3 \cdot \sqrt{\max\{\lambda_1, \lambda_2\}}$, where λ_1 and λ_2 denote the eigenvalues of the 2D covariance matrix $\Sigma'_{2 \times 2}$ (Sec. 4.1), will cover most of the function (main lobe), affecting the opacity modeling significantly. However, in our DARBFs, we have multiple side lobes which can have an undesirable effect on this bounding box unless the range is specified correctly. If these side lobes are included within the bounding box, each splat will have a ring effect in their opacity distributions.

To avoid this ring effect, we identified the range of the horizontal spread of the main lobe of each DARBF in terms of their Mahalanobis distance component and introduced a limit in opacity distribution to carefully remove the effects from their side lobes. In our Monte Carlo experiments (Sec. A.2), we used this limit in the 3D DARB kernel, as we directly perform the density calculation in 3D and the projection onto 2D image space afterwards. For example, let us consider the 3D raised cosine as follows:

$$w = 0.5 + 0.5 \cos\left(\frac{2\pi d_M^2}{5}\right) \quad (18)$$

where $\xi = \frac{5}{2\pi}$ and $\beta = 2$ according to the standard expression mentioned in Table 1. To avoid the side lobes and only use the main lobe, we assess the necessary range that we should consider with the Gaussian curves in 1D and chose the following limit (according to Table 1):

$$d_M^2 < 6.25 = \left(\pi \times \frac{5}{2\pi}\right)^2 \quad (19)$$

If the above limit is not satisfied by the Mahalanobis component, the density value will be taken as zero for those cases. As in the Table 1, this limit will be different for different DARBFs since each DARBF shows different characteristics regarding their spread, main lobe and side lobes. Applying these limits will help to consider the 100% support of the main lobe of each DARBF into the bounding box.

Even though we apply these limits on the 3D representation of each kernel and calculate the densities, in our reconstruction pipeline, we use these limits on DARB splats (2D) similar to 3DGS [11]. In our experiments, our main target was to identify the relationship between the 2D covariance $\Sigma'_{2 \times 2}$ and the 3D sub-matrix $\Sigma'_{3 \times 3}$ (Sec. A.2), and implement these limits on 3D DARB kernels.

B. DARB-Splatting Implementation

Here, we present the reconstruction kernel (3D) and splat (2D) functions (footprint functions) for selected DARBFs,

along with their respective derivative term modifications related to backpropagation, in both mathematical expressions and CUDA codes. These modifications have been incorporated into the splatting pipeline and CUDA code changes. In the code, d denotes $x - \mu'$, and $con = \begin{bmatrix} a & b \\ b & c \end{bmatrix}$ denotes the inverse of the 2D covariance matrix $(\Sigma'_{2 \times 2})^{-1}$ in the mathematical form. For each DARBF, we clearly show ξ and d_M in the code. We use a unique correction factor ψ for each DARBF, determined through Monte Carlo experiments, to compute $\Sigma'_{2 \times 2}$ from Σ' .

B.1. Raised Cosine Splatting

Here, a single pulse of the raised cosine signal is selected for enhanced performance. The 3D raised cosine function is as follows:

$$0.5 + 0.5 \cos\left(\frac{1}{\xi}(d_M)\right), \quad \frac{1}{\xi}(d_M) \leq \pi \quad (20)$$

The raised cosine splat function is as follows:

$$w = 0.5 + 0.5 \cos\left(\frac{\sqrt{(x - \mu')^T \Sigma'_{2 \times 2}^{-1} (x - \mu')}}{\xi}\right), \quad (21)$$

$$\frac{\sqrt{(x - \mu')^T \Sigma'_{2 \times 2}^{-1} (x - \mu')}}{\xi} \leq \pi$$

Modifications in derivative terms related to the raised cosine splat during backpropagation are provided next.

$$\frac{\partial w}{\partial (x - \mu')} = -\frac{0.5}{\xi} \sin\left(\frac{\sqrt{(x - \mu')^T \Sigma'_{2 \times 2}^{-1} (x - \mu')}}{\xi}\right) \cdot \frac{\Sigma'_{2 \times 2}^{-1} (x - \mu')}{\sqrt{(x - \mu')^T \Sigma'_{2 \times 2}^{-1} (x - \mu')}} \quad (22)$$

$$\frac{\partial w}{\partial \Sigma'_{2 \times 2}} = -\frac{0.5}{\xi} \sin\left(\frac{\sqrt{(x - \mu')^T \Sigma'_{2 \times 2}^{-1} (x - \mu')}}{\xi}\right) \cdot \frac{(x - \mu')(x - \mu')^T}{\sqrt{(x - \mu')^T \Sigma'_{2 \times 2}^{-1} (x - \mu')}} \quad (23)$$

The following CUDA code modifications were implemented to support raised cosine splatting.

```

1 float correctionFactor = 0.655f; // The correction
  factor we introduce
2 cov *= correctionFactor; // Multiply the 3D covariance
  matrix by the correction factor
3
4 float ellipse = con_o.x * d.x * d.x + con_o.z * d.y * d.
  y + 2.f * con_o.y * d.x * d.y; // dM**2
5 if (ellipse < 0 || ellipse > 6.25f) // Limit set on 2D
  ellipse to restrict to one pulse
6   continue;
7 float ellipse_root = sqrt(ellipse); // dM
8 float ellipseFactor = M_PI * ellipse_root / 2.5f; //
  Here scaling factor, xi = 5/(2 * math_pi)
9 const float Cosine = 0.5f + .5f * cos(ellipseFactor);
10 const float alpha = min(0.99f, con_o.w * Cosine); // w *
  raised cosine

```

Listing 1. Modifications in forward propagation in CUDA rasterizer for raised cosine splatting.

```

1 float correctionFactor = 0.655f;
2 cov2D *= correctionFactor;
3
4 // Gradients of loss w.r.t. entries of 2D covariance
  matrix,
5 // given gradients of loss w.r.t. conic matrix (inverse
  covariance matrix).
6 // e.g., dL / da = dL / d_conic_a * d_conic_a / da
7 dL_da = correctionFactor * denom2inv * (-c * c *
  dL_dconic.x + 2 * b * c * dL_dconic.y + (denom - a
  * c) * dL_dconic.z);
8 dL_dc = correctionFactor * denom2inv * (-a * a *
  dL_dconic.z + 2 * a * b * dL_dconic.y + (denom - a
  * c) * dL_dconic.x);
9 dL_db = correctionFactor * denom2inv * 2 * (b * c *
  dL_dconic.x - (denom + 2 * b * b) * dL_dconic.y + a
  * b * dL_dconic.z);
10
11 float ellipse = (con_o.x * d.x * d.x + con_o.z * d.y * d
  .y + 2.f * con_o.y * d.x * d.y);
12 if (ellipse < 0 || ellipse > 6.25f) // limit set on 2D
  ellipse to restrict to one pulse
13   continue;
14 float ellipse_root = sqrt(ellipse); // dM
15 float ellipseFactor = M_PI * ellipse_root / 2.5f;
16 const float Cosine = .5f + .5f * cos(ellipseFactor); //
  raised cosine
17 const float alpha = min(0.99f, con_o.w * Cosine); // w *
  raised cosine
18
19 // Helpful reusable temporary variables
20 const float dL_dCosine = con_o.w * dL_dalpha;
21 const float sindL_dCosine = sin(ellipseFactor) *
  dL_dCosine;
22 const float factor1 = -M_PI * sindL_dCosine / 5.f /
  ellipse_root;
23 const float factor2 = factor1 * 0.5;
24 const float dL_ddelx = (con_o.x * d.x + con_o.y * d.y) *
  factor1;
25 const float dL_ddely = (con_o.z * d.y + con_o.y * d.x) *
  factor1;
26
27 atomicAdd(&dL_dmean2D[global_id].x, dL_ddelx * ddelx_dx)
  ;
28 atomicAdd(&dL_dmean2D[global_id].y, dL_ddely * ddely_dy)
  ;
29 // Update gradients w.r.t. 2D covariance (2x2 matrix,
  symmetric)
30 atomicAdd(&dL_dconic2D[global_id].x, d.x * d.x * factor2
  );
31 atomicAdd(&dL_dconic2D[global_id].y, d.x * d.y * factor2
  );
32 atomicAdd(&dL_dconic2D[global_id].w, d.y * d.y * factor2
  );
33 // Update gradients w.r.t. opacity of the Cosine
34 atomicAdd(&(dL_dopacity[global_id]), Cosine * dL_dalpha)
  ;

```

Listing 2. Modifications in backward propagation in CUDA rasterizer for raised cosine splatting.

B.2. Half-cosine Squared Splatting

The 3D half-cosine square function we selected is as follows:

$$\cos\left(\frac{1}{\xi}(d_M)^2\right), \quad \frac{1}{\xi}(d_M)^2 \leq \frac{\pi}{2}$$

The corresponding half-cosine squared splat function is as follows:

$$w = \cos\left(\frac{(x - \mu')^T (\Sigma'_{2 \times 2})^{-1} (x - \mu')}{\xi}\right), \quad (24)$$

$$\frac{\sqrt{(x - \mu')^T \Sigma'_{2 \times 2}^{-1} (x - \mu')}}{\xi} \leq \frac{\pi}{2}$$

Adjustments to the derivative terms associated with the half-cosine squared splat during backpropagation are given below.

$$\frac{dw}{d(x - \mu')} = \frac{-2(\Sigma'_{2 \times 2})^{-1} (x - \mu') \sin\left(\frac{(x - \mu')^T (\Sigma'_{2 \times 2})^{-1} (x - \mu')}{\xi}\right)}{\xi} \quad (25)$$

$$\frac{dw}{d((\Sigma'_{2 \times 2})^{-1})} = \frac{-(x - \mu') (x - \mu')^T \sin\left(\frac{(x - \mu')^T (\Sigma'_{2 \times 2})^{-1} (x - \mu')}{\xi}\right)}{\xi} \quad (26)$$

The following CUDA code changes were made to support half-cosine squared splatting.

```

1 float correctionFactor = 1.36f; // The correction
  factor we introduce
2 cov *= correctionFactor; // Multiply the 3D covariance
  matrix by the correction factor
3
4 float ellipse = con_o.x * d.x * d.x + con_o.z * d.y * d
  .y + 2.f * con_o.y * d.x * d.y; // dm_squared
5 if (ellipse < 0.f || ellipse > 9.f) // limit set on 2D
  ellipse to restrict half cosine pulse
6   continue;
7 float ellipseFactor = 0.175f * ellipse; // 2 * M_PI *
  ellipse / 36;
8 const float Cosine = cos(ellipseFactor);
9 const float alpha = min(0.99f, con_o.w * Cosine); // w *
  cosine

```

Listing 3. Modifications in forward propagation in CUDA rasterizer for half-cosine squared splatting.

```

1 float correctionFactor = 1.36f;
2 cov2D *= correctionFactor;
3
4 // Gradients of loss w.r.t. entries of 2D covariance
  matrix,
5 // given gradients of loss w.r.t. conic matrix (inverse
  covariance matrix).
6 // e.g., dL / da = dL / d_conic_a * d_conic_a / da
7 dL_da = correctionFactor * denom2inv * (-c * c *
  dL_dconic.x + 2 * b * c * dL_dconic.y + (denom - a
  * c) * dL_dconic.z);
8 dL_dc = correctionFactor * denom2inv * (-a * a *
  dL_dconic.z + 2 * a * b * dL_dconic.y + (denom - a
  * c) * dL_dconic.x);
9 dL_db = correctionFactor * denom2inv * 2 * (b * c *
  dL_dconic.x - (denom + 2 * b * b) * dL_dconic.y + a
  * b * dL_dconic.z);
10
11 float ellipse = con_o.x * d.x * d.x + con_o.z * d.y * d
  .y + 2.f * con_o.y * d.x * d.y;
12 if (ellipse < 0 || ellipse > 9.f) // limit set on 2D
  ellipse
13   continue;
14 float ellipseFactor = 0.174f * ellipse; // 2 * M_PI *
  ellipse / 36.f;
15 const float Cosine = cos(ellipseFactor); // half cosine
  square
16 const float alpha = min(0.99f, con_o.w * Cosine);
17
18 // Helpful reusable temporary variables
19 const float dL_dCosine = con_o.w * dL_dalpha;
20 const float sindL_dCosine = -0.349 * sin(ellipseFactor) *
  dL_dCosine;

```

```

21 const float halfsindL_dCosine = 0.5f * sindL_dCosine;
22 const float dCosine_ddelx = ( con_o.x * d.x + con_o.y *
    d.y) * sindL_dCosine ;
23 const float dCosine_ddely = ( con_o.z * d.y + con_o.y *
    d.x) * sindL_dCosine;
24
25 // Update gradients w.r.t. 2D mean position of the half
    cosine squared
26 atomicAdd(&dL_dmean2D[global_id].x, dCosine_ddelx *
    ddelx_dx);
27 atomicAdd(&dL_dmean2D[global_id].y, dCosine_ddely *
    ddely_dy);
28 // Update gradients w.r.t. 2D covariance (2x2 matrix,
    symmetric)
29 atomicAdd(&dL_dconic2D[global_id].x, d.x * d.x *
    halfsindL_dCosine);
30 atomicAdd(&dL_dconic2D[global_id].y, d.x * d.y *
    halfsindL_dCosine );
31 atomicAdd(&dL_dconic2D[global_id].w, d.y * d.y *
    halfsindL_dCosine);
32 // Update gradients w.r.t. opacity of the half cosine
    squared
33 atomicAdd(&(dL_dopacity[global_id]), Cosine * dL_dalpha)
    ;

```

Listing 4. Modifications in backward propagation in CUDA rasterizer for half-cosine squared splatting.

B.3. Sinc Splatting

Here, the sinc function refers to a single pulse of the modulus sinc function. This configuration was selected due to improved performance. The corresponding 3D sinc function is provided below:

$$\left| \frac{\sin\left(\frac{1}{\xi}(d_M)\right)}{\frac{1}{\xi}(d_M)} \right|, \quad \frac{1}{\xi}(d_M) \leq \pi$$

The related sinc splat function is as follows:

$$w = \frac{\left| \sin\left(\frac{\sqrt{(x-\mu')^T (\Sigma'_{2 \times 2})^{-1} (x-\mu')}}{\xi}\right) \right|}{\left(\frac{\sqrt{(x-\mu')^T (\Sigma'_{2 \times 2})^{-1} (x-\mu')}}{\xi} \right)}, \quad (27)$$

$$\frac{\sqrt{(x-\mu')^T \Sigma'^{-1}_{2 \times 2} (x-\mu')}}{\xi} \leq \pi$$

The modifications to the derivative terms related to the sinc splat in backpropagation are outlined below.

$$\frac{\partial w}{\partial (x-\mu')} = \text{sgn}\left(\frac{\sin(A)}{A}\right) \cdot \frac{A \cos(A) - \sin(A)}{A^2} \cdot \frac{2(\Sigma'_{2 \times 2})^{-1} (x-\mu')}{\xi}, \quad (28)$$

$$\frac{\partial w}{\partial (\Sigma'_{2 \times 2})^{-1}} = \text{sgn}\left(\frac{\sin(A)}{A}\right) \cdot \frac{A \cos(A) - \sin(A)}{A^2} \cdot \frac{(x-\mu')(x-\mu')^T}{\xi}, \quad (29)$$

where $A = \frac{(x-\mu')^T (\Sigma'_{2 \times 2})^{-1} (x-\mu')}{\xi}$.

The following CUDA code changes were made to support the sinc splatting described here.

```

1 float correctionFactor = 1.18f; // The correction
    factor we introduce
2 cov **= correctionFactor; // Multiply the 3D covariance
    matrix by the correction factor
3
4 float constA = 3.0f/ M_PI;
5 float ellipse = con_o.x * d.x * d.x + con_o.z * d.y * d.
    y + 2.f * con_o.y * d.x * d.y; // dM**2
6 if (ellipse <= 0 || ellipse > 9.f) // limit set on 2D
    ellipse to restrict to one pulse
7     continue;
8 float ellipse_root = sqrt(ellipse); // dM
9 float ellipse_rootdivA = ellipse_root / constA;
10 float alpha = min(0.99f, con_o.w * fabs(sin(
    ellipse_rootdivA) / ellipse_rootdivA)); // w *
    modulus sinc

```

Listing 5. Modifications in forward propagation in CUDA rasterizer for sinc splatting.

```

1 float correctionFactor = 1.18f;
2 cov2D **= correctionFactor;
3
4 // Gradients of loss w.r.t. entries of 2D covariance
    matrix,
5 // given gradients of loss w.r.t. conic matrix (inverse
    covariance matrix).
6 // e.g., dL / da = dL / d_conic_a * d_conic_a / d_a
7 dL_da = correctionFactor * denom2inv * (-c * c *
    dL_dconic.x + 2 * b * c * dL_dconic.y + (denom - a
    * c) * dL_dconic.z);
8 dL_dc = correctionFactor * denom2inv * (-a * a *
    dL_dconic.z + 2 * a * b * dL_dconic.y + (denom - a
    * c) * dL_dconic.x);
9 dL_db = correctionFactor * denom2inv * 2 * (b * c *
    dL_dconic.x - (denom + 2 * b * b) * dL_dconic.y + a
    * b * dL_dconic.z);
10
11 float constA = 3.0f/ M_PI;
12 float ellipse = con_o.x * d.x * d.x + con_o.z * d.y * d.
    y + 2.f * con_o.y * d.x * d.y;
13 if (ellipse <= 0 || ellipse > 9.f) // limit set on 2D
    ellipse to restrict to one pulse
14     continue;
15 float ellipse_root = sqrt(ellipse); // dM
16 float ellipse_rootdivA = ellipse_root / constA;
17 const float sinellipse_rootdivA = sin(ellipse_rootdivA);
18 const float G = fabs(sinellipse_rootdivA /
    ellipse_rootdivA); // modulus sinc
19 const float alpha = min(0.99f, con_o.w * G); // w *
    modulus sinc
20
21 // Helpful reusable temporary variables
22 const float dL_dG = con_o.w * dL_dalpha;
23 // Original equation:
24 // cospart = cos(ellipse_rootdivA) * sin(
    ellipse_rootdivA) * fabs(1 / ellipse_root) /
    ellipse_root / fabs(sin(ellipse_rootdivA))
25 // Simplified equation using copysignf for clarity:
26 const float cospart = cos(ellipse_rootdivA) * copysignf
    (1.0f, sinellipse_rootdivA) / ellipse ;
27 const float sinpart = constA * fabs(sinellipse_rootdivA)
    / ellipse / ellipse_root ;
28 const float commonpart = (cospart - sinpart) * dL_dG;
29 const float commonpartdiv2 = commonpart * 0.5f;
30 const float dG_ddelx = commonpart * (d.x * con_o.x + d.y
    * con_o.y);
31 const float dG_ddely = commonpart * (d.x * con_o.y + d.y
    * con_o.z);
32 // Update gradients w.r.t. 2D mean position of the
    modulus sinc
33 atomicAdd(&dL_dmean2D[global_id].x, dG_ddelx * ddelx_dx)
    ;
34 atomicAdd(&dL_dmean2D[global_id].y, dG_ddely * ddely_dy
    );
35 // Update gradients w.r.t. 2D covariance (2x2 matrix,
    symmetric)

```

```

36 atomicAdd(&dL_dconic2D[global_id].x, commonpartdiv2 * d.
    x * d.x );
37 atomicAdd(&dL_dconic2D[global_id].y, commonpartdiv2 * d.
    x * d.y );
38 atomicAdd(&dL_dconic2D[global_id].w, commonpartdiv2 * d.
    y * d.y );
39 // Update gradients w.r.t. opacity of the modulus sinc
40 atomicAdd(&(dL_dopacity[global_id]), G * dL_dalpha);

```

Listing 6. Modifications in backward propagation in CUDA rasterizer for sinc splatting.

B.4. Inverse Multiquadric Splatting

Here, we define the inverse multiquadric formulation based on the following 3D inverse multiquadric function:

$$\frac{1}{\left[\frac{1}{\xi}(d_M)^2 + 1\right]}, \quad d_M \geq 0$$

The corresponding inverse multiquadric splat function is as follows:

$$w = \frac{1}{\left[\frac{1}{\xi}(x - \mu')^T (\Sigma'_{2 \times 2})^{-1} (x - \mu') + 1\right]} \quad (30)$$

The changes done to the derivative terms related to the inverse multiquadric splat during backpropagation are detailed below.

$$\frac{\partial w}{\partial z} = -\frac{2}{\xi \left(\frac{1}{\xi} z^T (\Sigma'_{2 \times 2})^{-1} z + 1\right)^2} (\Sigma'_{2 \times 2})^{-1} z. \quad (31)$$

$$\frac{\partial w}{\partial (\Sigma'_{2 \times 2})^{-1}} = -\frac{1}{\left(\frac{1}{\xi} z^T (\Sigma'_{2 \times 2})^{-1} z + 1\right)^2} \cdot \frac{1}{\xi} z z^T. \quad (32)$$

where $z = (x - \mu')$.

The CUDA code modifications provided below were implemented to enable the inverse multiquadric splatting described in this section.

```

1 float correctionFactor = 1.38f; // The correction
    factor we introduce
2 cov *= correctionFactor; // Multiply the 3D covariance
    matrix by the correction factor
3
4 float ellipse = con_o.x * d.x * d.x + con_o.z * d.y * d.
    y + 2.f * con_o.y * d.x * d.y; // dm**2
5 if (ellipse <= 0)
6     continue;
7 if (ellipse >= 9.f) // limit set on 2D ellipse
8     continue;
9 float alpha = min(0.99f, con_o.w * (1.f / (ellipse + 1.f
    ))); // w * inverse quadric

```

Listing 7. Modifications in forward propagation in CUDA rasterizer for inverse multiquadric splatting.

```

1 float correctionFactor = 1.38f;
2 cov2D *= correctionFactor;
3
4 // Gradients of loss w.r.t. entries of 2D covariance
    matrix,

```

```

5 // given gradients of loss w.r.t. conic matrix (inverse
    covariance matrix).
6 // e.g., dL / da = dL / d_conic_a * d_conic_a / d_a
7 dL_da = correctionFactor * denom2inv * (-c * c *
    dL_dconic.x + 2 * b * c * dL_dconic.y + (denom - a
    * c) * dL_dconic.z);
8 dL_dc = correctionFactor * denom2inv * (-a * a *
    dL_dconic.z + 2 * a * b * dL_dconic.y + (denom - a
    * c) * dL_dconic.x);
9 dL_db = correctionFactor * denom2inv * 2 * (b * c *
    dL_dconic.x - (denom + 2 * b * b) * dL_dconic.y + a
    * b * dL_dconic.z);
10
11 float ellipse = con_o.x * d.x * d.x + con_o.z * d.y * d.
    y + 2.f * con_o.y * d.x * d.y;
12 if (ellipse <= 0)
13     continue;
14 if (ellipse >= 9.f) // limit set on 2D ellipse
15     continue;
16 const float G = (1.f / (ellipse + 1.f)); // inverse
    quadric
17 const float alpha = min(0.99f, con_o.w * G);
18
19 // Helpful reusable temporary variables
20 const float dL_dG = con_o.w * dL_dalpha;
21 const float ellipsepow = -dL_dG * 2.f / pow(ellipse +
    1.f, 2.f);
22 const float halfellipsepow = 0.5f * ellipsepow;
23 const float dG_ddelx = ellipsepow * (d.x * con_o.x + d.y
    * con_o.y);
24 const float dG_ddely = ellipsepow * (d.x * con_o.y + d.y
    * con_o.z);
25 // Update gradients w.r.t. 2D mean position of the IQF
26 atomicAdd(&dL_dmean2D[global_id].x, dG_ddelx * ddelx_dx
    );
27 atomicAdd(&dL_dmean2D[global_id].y, dG_ddely * ddely_dy
    );
28 // Update gradients w.r.t. 2D covariance (2x2 matrix,
    symmetric)
29 atomicAdd(&dL_dconic2D[global_id].x, halfellipsepow * d.
    x * d.x );
30 atomicAdd(&dL_dconic2D[global_id].y, halfellipsepow * d.
    x * d.y );
31 atomicAdd(&dL_dconic2D[global_id].w, halfellipsepow * d.
    y * d.y );
32 // Update gradients w.r.t. opacity of the IQF
33 atomicAdd(&(dL_dopacity[global_id]), G * dL_dalpha);

```

Listing 8. Modifications in backward propagation in CUDA rasterizer for inverse multiquadric splatting.

B.5. Parabolic Splatting

Here, we define the parabolic formulation based on the following 3D parabolic function:

$$1 - \frac{1}{\xi}(d_M)^2, \quad d_M \geq 0$$

The corresponding parabolic splat function is as follows:

$$w = \left[1 - \frac{1}{\xi}(x - \mu')^T (\Sigma'_{2 \times 2})^{-1} (x - \mu')\right] \quad (33)$$

The changes done to the derivative terms related to the parabolic splat during backpropagation are detailed below.

$$\frac{\partial w}{\partial z} = -\frac{2}{\xi} (\Sigma'_{2 \times 2})^{-1} z. \quad (34)$$

$$\frac{\partial w}{\partial (\Sigma'_{2 \times 2})^{-1}} = -\frac{1}{\xi} z z^T \quad (35)$$

where $z = (x - \mu')$.

The CUDA code modifications provided below were implemented to enable the parabolic splatting described in this section.

```

1 float correctionFactor = 1.3f;
2 cov *= correctionFactor ;
3
4 float ellipse = (con_o.x * d.x * d.x + con_o.z * d.y * d
   .y + 2.f * con_o.y * d.x * d.y); //dM**2
5
6 if (ellipse < 0 || ellipse > 9.f)
7     continue;
8
9 const float parabola = 1. - ellipse / 9.;
10 const float alpha = min(0.99f, con_o.w * parabola);

```

Listing 9. Modifications in forward propagation in CUDA rasterizer for parabolic splatting.

```

1 float correctionFactor = 1.3f;
2 cov2D *= correctionFactor ;
3
4 // Gradients of loss w.r.t. entries of 2D covariance
   matrix,
5 // given gradients of loss w.r.t. conic matrix (inverse
   covariance matrix).
6 // e.g., dL / da = dL / d_conic_a * d_conic_a / d_a
7 dL_da = denom2inv * (-c * c * dL_dconic.x + 2 * b * c *
   dL_dconic.y + (denom - a * c) * dL_dconic.z);
8 dL_dc = denom2inv * (-a * a * dL_dconic.z + 2 * a * b *
   dL_dconic.y + (denom - a * c) * dL_dconic.x);
9 dL_db = denom2inv * 2 * (b * c * dL_dconic.x - (denom +
   2 * b * b) * dL_dconic.y + a * b * dL_dconic.z);
10
11 float ellipse = (con_o.x * d.x * d.x + con_o.z * d.y * d
   .y + 2.f * con_o.y * d.x * d.y);
12
13
14 if (ellipse < 0 || ellipse > 9.f)
15     continue;
16
17 const float parabola = 1. - ellipse / 9.;
18 const float alpha = min(0.99f, con_o.w * parabola);
19
20 // Helpful reusable temporary variables
21 const float dL_dP = con_o.w * dL_dalpha;
22 const float dP_ddelx = ( con_o.x * d.x + con_o.y * d.y) *
   -2. / 9.;
23 const float dP_ddely = ( con_o.z * d.y + con_o.y * d.x) *
   -2. / 9.;
24
25 atomicAdd(&dL_dmean2D[global_id].x, dL_dP * dP_ddelx *
   ddelx_dx);
26 atomicAdd(&dL_dmean2D[global_id].y, dL_dP * dP_ddely *
   ddely_dy);
27 // Update gradients w.r.t. 2D covariance (2x2 matrix,
   symmetric)
28
29 atomicAdd(&dL_dconic2D[global_id].x, dL_dP * d.x * d.x
   / -9.f);
30 atomicAdd(&dL_dconic2D[global_id].y, dL_dP * d.x * d.y
   / -9.f);
31 atomicAdd(&dL_dconic2D[global_id].w, dL_dP * d.y * d.y
   / -9.f);
32
33 // Update gradients w.r.t. opacity of the Cosine
34 atomicAdd(&(dL_dopacity[global_id]), parabola *
   dL_dalpha);

```

Listing 10. Modifications in backward propagation in CUDA rasterizer for parabolic splatting.

C. Utility Applications of DARB-Splatting

C.1. Enhanced Quality

In terms of splatting, despite Gaussians providing SOTA quality, we demonstrate that the raised cosine function can deliver modestly improved visual quality compared to Gaussians. Our 1D simulations, presented in Sec. A.1 and Sec. D, and the qualitative visual comparisons demonstrated in Fig. 7, illustrate this effectively.

Across the selected DARBFs, only the raised cosine outperforms the Gaussian in terms of quality, albeit by a small margin. The others fail to surpass the Gaussian in terms of quality. The primary reason is that exponentially decaying functions ensure faster blending compared to relatively flatter functions. However, these functions have other utilities, which we will discuss next.

C.2. Reduced Training Time

According to Fig. 5, which shows the half-cosine square with $\beta = 2$ and $\xi = 36$, along with the Gaussian 1D plot, we can observe that for a single primitive with the same variance, the cosine function can provide higher opacity values. Instead of requiring multiple splats to composite to determine the final pixel color, the cosine function can achieve the same accumulated value required with fewer primitives. Although the cosine function’s computation is more time-intensive compared to the Gaussian calculations, the overall training time is reduced due to the lower number of primitives required.

This is further illustrated in Figures 8 and 9, which provide a detailed analysis of the training loss and speed curves across various dataset scenes. Overall, despite having similar training loss curves with 3DGS, half-cosine splatting demonstrates superior performance compared to Gaussians.

C.3. Reduced Memory Usage

As previously mentioned, half cosine squared splatting specifically requires fewer primitives compared to Gaussians. This results in lower memory usage, as they provide higher opacity values across most of the regions they cover. In contrast, Gaussians require more primitives to achieve a similar accumulated opacity coverage. By using fewer half cosine squared primitives, we can achieve the desired color representation in the image space more efficiently. Similarly, sinc splatting and inverse multiquadric splatting also consume lesser memory compared to Gaussians. The results in Table 11 and Table 12 further showcase this.

D. Extended Results and Simulations

Extended Results. As mentioned in our paper, we trained our models on a single NVIDIA GeForce RTX 4090 GPU and recorded the training time. Since the benchmark



Figure 7. **Qualitative Visualization Across 3DGS and raised cosine splatting.** Displayed are side-by-side comparisons across the Counter, Truck, DrJohnson, Bonsai scenes (top to bottom) respectively from Mip-NeRF 360, Tanks&Temples and Deep Blending datasets. In the Counter scene, raised cosines outperform Gaussians by better reconstructing the buttons, rendering them more prominently, whereas Gaussians struggle to achieve this even after full training. Similarly, in the Truck scene, raised cosines successfully reconstruct the orange mark on the floor, a detail that Gaussians fail to capture. In the Dr. Johnson scene, our method renders the string of the picture frame with greater clarity, closely resembling the ground truth imagery, while Gaussians fail to achieve the same level of detail. Lastly, in the Bonsai scene, the edges of the pot are more accurately represented by raised cosines as we can see its shadows, producing results that are closer to the ground truth image compared to those achieved with Gaussians. These examples highlight the advantages of raised cosine splatting in capturing finer details in 3D reconstruction compared to Gaussians.

models from other papers [10, 11] were trained on different GPUs, we applied a scaling factor to ensure a fair comparison of training times with the *original* papers’ results. According to [28], the relative training throughput of the RTX 4090 GPU and other GPU models (specifically, the RTX 3090 and RTX A6000 GPUs) can be determined with respect to a 1xLambdaCloud V100 16GB GPU. By dividing

the training time data by these values, we have presented our training time results in a fair and comparable manner in Table 3.

A detailed breakdown of our results across every scene in the Mip-NeRF 360 [12], Tanks&Temples [26], and Deep Blending [19] datasets, along with their average values per dataset, is provided in Table 11 and Table 12. These results

pertain to the selected DARB-Splatting algorithms, namely raised cosine splatting (3DRCS), half-cosine squared splatting (3DHCS), sinc splatting (3DSS), and inverse multi-quadric splatting (3DIQS). Key evaluation metrics, including PSNR, SSIM, LPIPS, memory usage, and training time for both 7k and 30k iterations, are analyzed in detail. These are presented alongside the results from implementing the *updated codebase* of 3DGS on our single NVIDIA GeForce RTX 4090 GPU to ensure a fair comparison. Our pipeline is anchored on this *updated codebase*, which produces improved results compared to those reported in the original 3DGS paper [11]. As shown in the tables, each DARB-Splatting algorithm demonstrates unique advantages in different utilities.

Function	Loss ($N = 5$)	Loss ($N = 10$)
Gaussian	0.0002	0.0001
Modified half cosine	0.0014	0.0003
Modified raised cosine	0.0002	0.00004*
Modified sinc (modulus)	0.0030	0.0002

Table 7. Comparison of 1D simulation results with Gaussian components vs. other reconstruction kernel components. Note that * indicates that we achieved better reconstruction with fewer components ($N = 8$) in terms of mean squared error, using our modified raised cosine pulses compared to Gaussians.

1D Simulations. In Figures 10, 11, 12, 13, 14, 15, 16, we show an extended version of the initial 1D simulation described in Sec. A.1 in our paper. Here, we conduct experiments with various reconstruction kernels in 1D as a toy experiment to understand their signal reconstruction properties. These kernels include Gaussians, cosines, squared cosines, raised cosines, squared raised cosines, and modulus sines. The reconstruction process is optimized using backpropagation, with different means and variances applied to each kernel. This approach is used to reconstruct various complex signal types, including a square pulse, a triangular pulse, a Gaussian pulse, a half-sinusoid single pulse, a sharp exponential pulse, a parabolic pulse, and a trapezoidal pulse.

We are grateful to the authors of GES [10] for open-sourcing their 1D simulation codes, which we have improved upon for this purpose. Expanding beyond GES, here, we also demonstrate the reconstruction of non-symmetric 1D signals to better represent real-world 3D reconstructions and further explore the capabilities of various DARBs. As shown in the simulations, Gaussians are not the only effective interpolators; other DARBs can provide improved 1D signal reconstructions in specific cases. We generate synthetic 3D covariance matrices that align with the properties of actual 3D covariances in the Gaussian Splatting pipeline. These matrices satisfy three key properties: (1) they are symmetric, (2) they are positive semi-definite, and (3) they have full rank. From these, we derive

the actual 2D covariances, as proposed in [82], by removing the last row and column of the 3D covariance matrices. Additionally, we obtain the projected 2D covariances by integrating along one axis using Simpson’s rule.

To approximate the relationship between these projected 2D covariances and the actual 2D covariances defined in [82], we train a single-layer Multi-Layer Perceptron (MLP). Through extensive experiments, we observed that this MLP model can be closely approximated by a linear regression model. Furthermore, the correction factor ψ can be simplified to a scalar value. We input 6 unique variables ($a, b, c, d, e,$ and f) derived from the 3D covariance and model the 3 unique outputs (a', b' and d') from the 2D covariance.

$$\Sigma' = \begin{pmatrix} a & b & c \\ b & d & e \\ e & d & f \end{pmatrix} \rightarrow \begin{pmatrix} a' & b' \\ b' & d' \end{pmatrix} = \Sigma'_{2 \times 2}. \quad (36)$$

The results we obtained using 1000 random samples, similar to the 3D covariances from 3DGS, are as follows:

$$a' = 1.36a - 0.2b - 0.1c - 0.0d + 0.0e + 0.0f \quad (37)$$

$$b' = 0.0a + 1.36b - 0.0c - 0.0d + 0.0e + 0.0f \quad (38)$$

$$d' = 0.0a + 0.0b - 0.2c + 1.36d + 0.1e + 0.0f \quad (39)$$

Experiments show that only the direct 3D covariance elements corresponding to the 2D covariance elements have higher weights, which can be represented as a single factor. A detailed statistical analysis using T-tests revealed distinct differences, highlighting the influence of weights on specific components of the 2D covariance matrix.

$$\Sigma' = \begin{pmatrix} a & b & c \\ b & d & e \\ e & d & f \end{pmatrix} \rightarrow \psi \begin{pmatrix} a & b \\ b & d \end{pmatrix} = \Sigma'_{2 \times 2}. \quad (40)$$

LR	PSNR		Training Time		Memory	
	Gaussian	HCS	Gaussian	HCS	Gaussian	HCS
0.01	31.49	31.335	22:31	23:26	255.61	246.48
0.02	31.75	31.34	19:48	17:32	293.61	282.65
0.1	31.1	29.38	13:31	11:20	364	391.76
0.2	30.5	26.54	10:34	8:26	241.42	315.93

Table 8. Comparison of Gaussian and HCS methods based on PSNR, Training Time, and Memory usage for different learning rates.

By formulating this as a regression problem and applying closed-form solutions, we determined the scalar correlation

Method	SSIM \uparrow	PSNR \uparrow	LPIPS \downarrow	Train \downarrow
Plenoxels [14]	0.626	23.08	0.463	19m*
INGP [41]	0.699	25.59	0.331	5.5m*
Mip-NeRF360 [12]	0.792	27.69	0.237	48h
3DGS [11]	0.815	27.21	0.214	30m*
GES [10]	0.794	26.91	0.250	23m*
DARBS (RC)	0.813	27.45	0.214	19min
DARBS (HC)	0.790	27.04	0.247	16min

Table 9. Comparison with prior methods in 3D reconstruction methods in PSNR, LPIPS, and training efficiency. Benchmark values for 3DGS and GES are from their respective papers and may not ensure a fully fair comparison.

Scene (Mip-NeRF 360 dataset)	RTX 3090		RTX 4090	
	Gaussian	HC	Gaussian	HC
Kitchen	32m 15s	29m 59s	21m 53s	19m 41s
Room	28m 32s	25m 28s	19m 48s	17m 32s

Table 10. Performance comparison of Gaussian and half-cosine (HC) methods on RTX 3090 and RTX 4090 for different environments. Even with upgraded computational capabilities, our results indicate that half-cosine kernels achieve better training speeds compared to Gaussian kernels.

factor for each DARBF. The scalar approximations for each kernel are presented in the original paper in Table 2.

Convergence Experiments. We acknowledge that the objective function remains Lipschitz continuous, as the smoothness induced by each reconstruction kernel may vary. The Table 8 above presents the convergence behavior for different learning rates. Neither reconstruction kernel achieves optimal performance at excessively high or low learning rates.

Cosine kernels do not induce smoothness to the same extent as Gaussian kernels. At higher learning rates, cosine-based reconstructions may perform worse than Gaussian-based ones. However, at optimal learning rates, the inherent properties of cosine kernels—such as their steeper roll-off, sparse gradients due to the blunt peak, and spatial constraints—enable them to achieve competitive visual quality and faster convergence compared to Gaussian kernels.

As this is the first study exploring the behavior of non-exponential kernels in this context, a detailed mathematical analysis remains beyond the scope of this work. However, we identify opportunities for future research to further investigate the mathematical properties of these kernels through rigorous analytical methods.

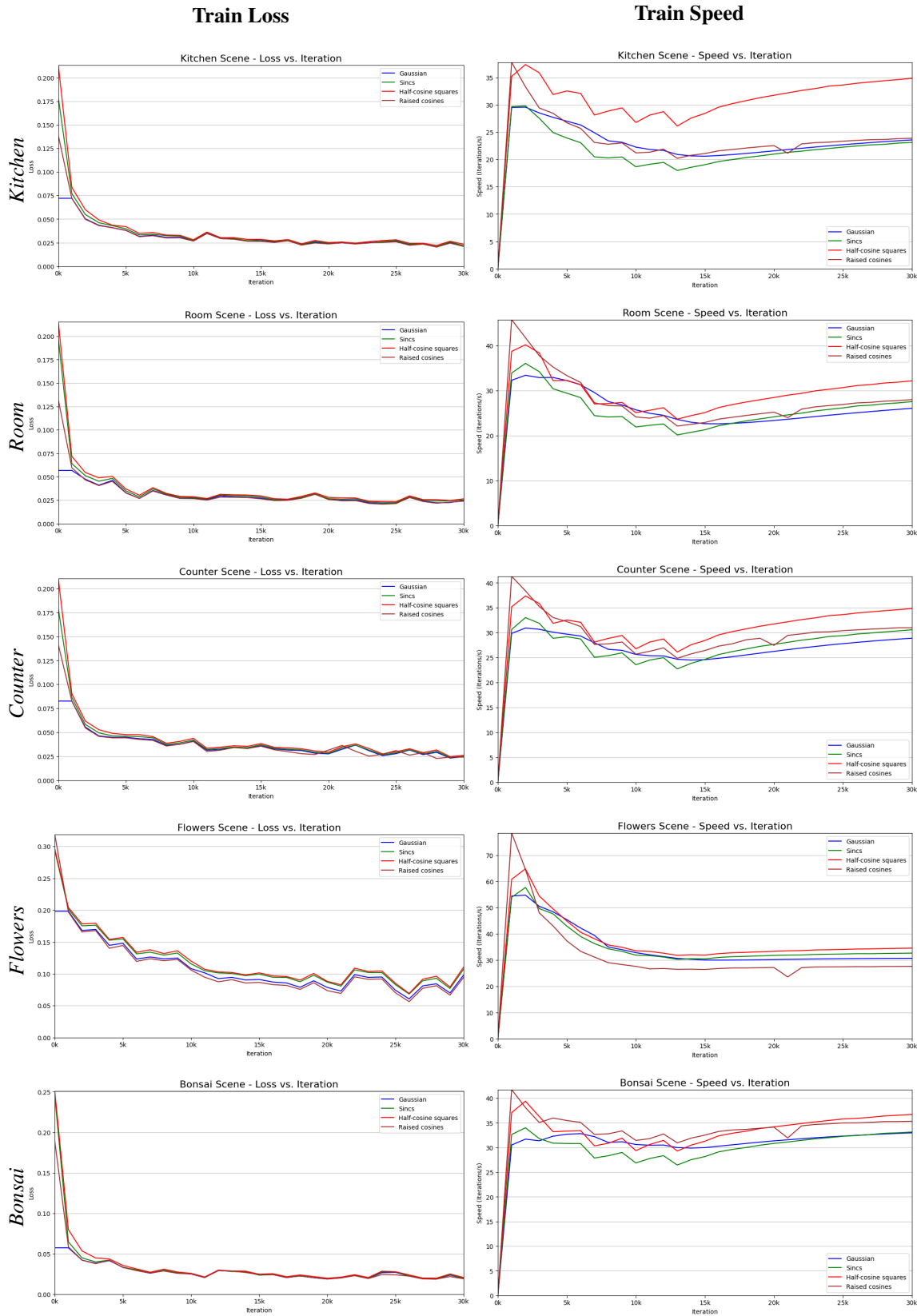


Figure 8. Training loss and speed curves across different scenes reveal significant performance differences. Specifically, the superior convergence speed of half-cosine squared splatting stands out compared to other selected DARBFs, particularly the Gaussian function. Although all the selected functions exhibit similar loss curves, notable variations are observed in their respective training speed curves across various scenes. These differences can be attributed to the inherent characteristics of each scene, which influence the training dynamics of the functions.

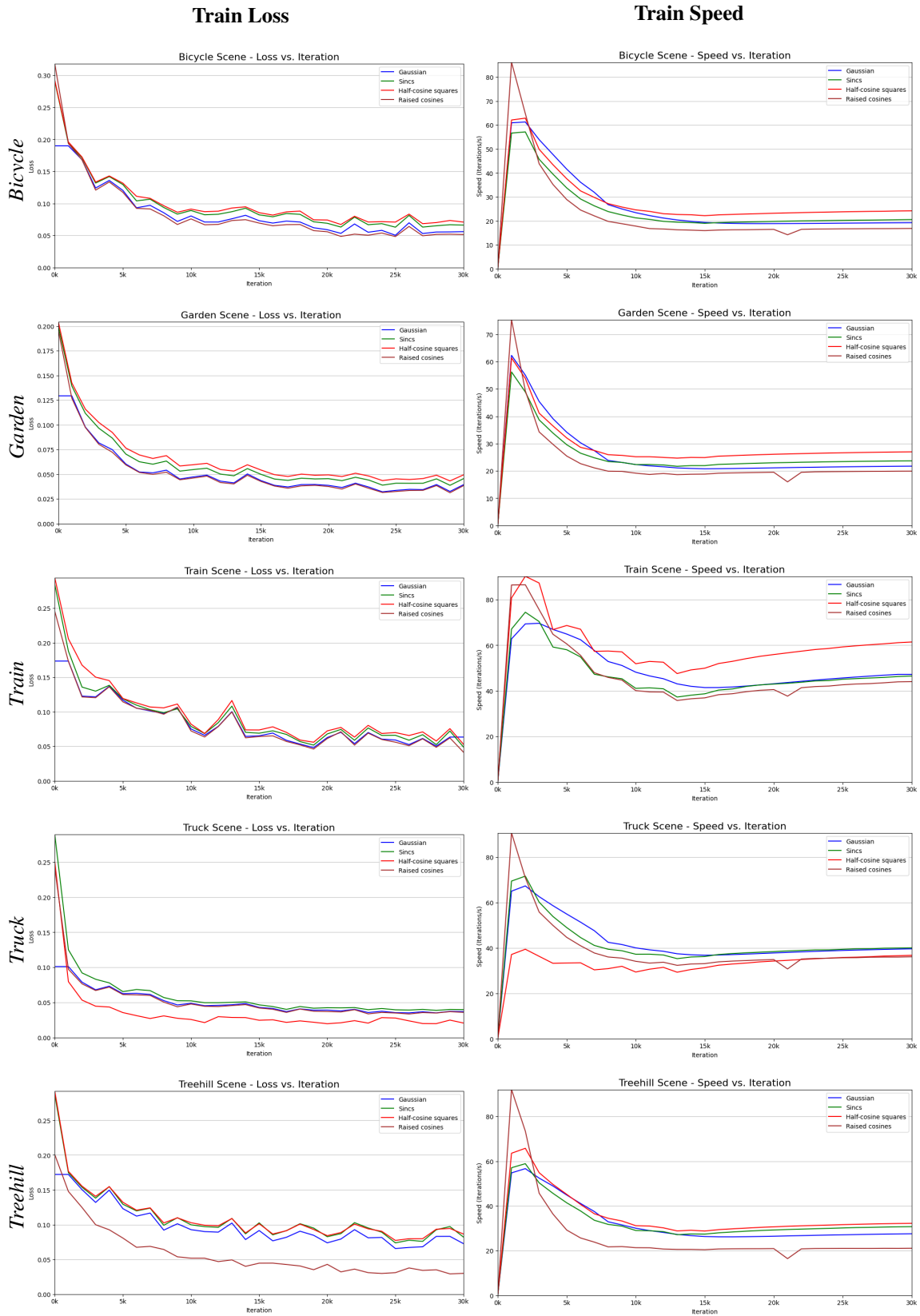


Figure 9. Training loss and speed curves across different scenes reveal significant performance differences. As an exception, in the Truck scene, we observe that the speed curves of Gaussians and raised cosines overlap and outperform half-cosine squares. However, when considering the overall performance across all scenes, half-cosine squares demonstrates superior efficiency in training time.

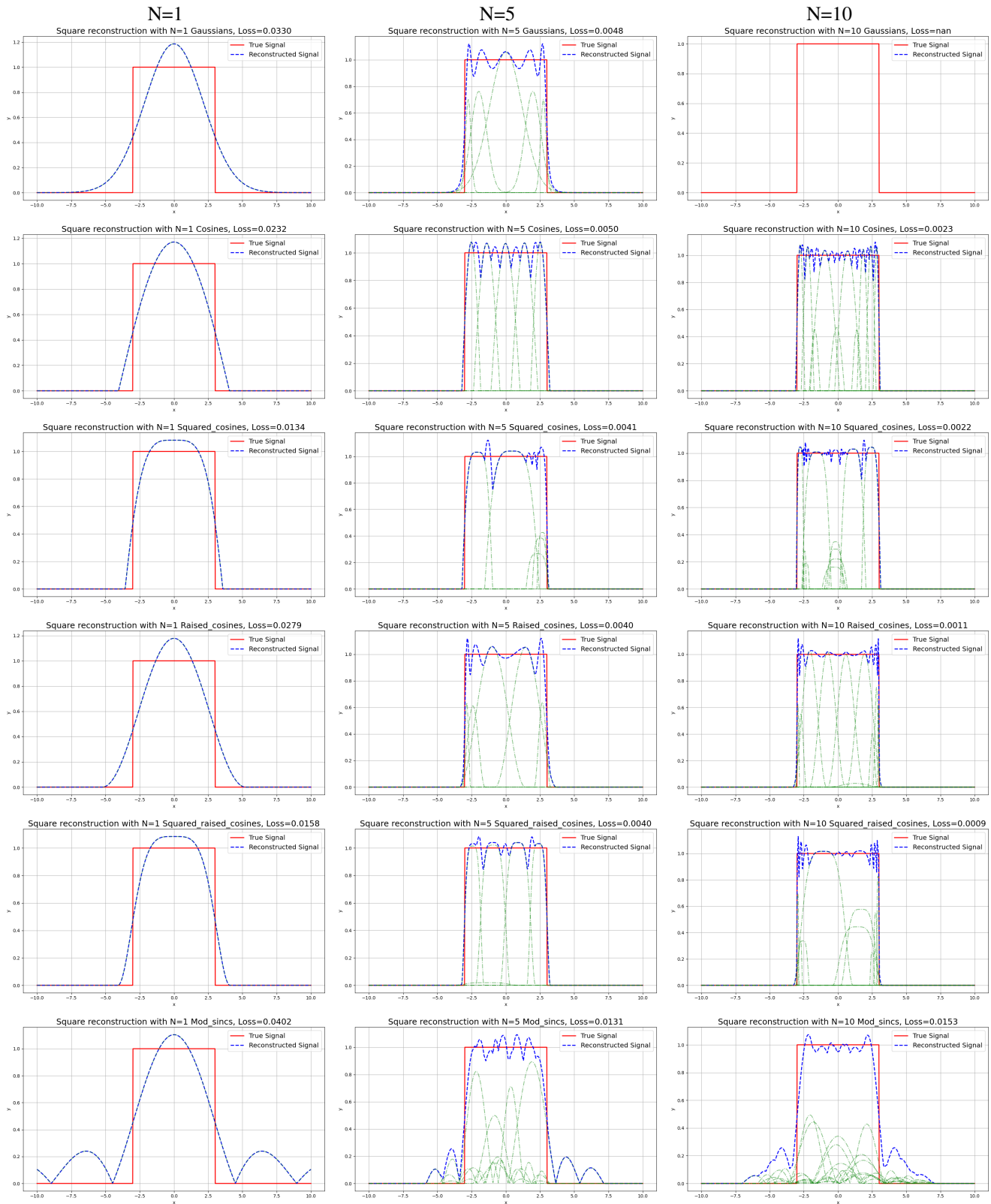


Figure 10. Visualization of 1D simulations for different splatting methods with varying primitives (N=1, N=5, N=10) for a square pulse. Each row corresponds to a specific splatting method: Gaussian, Cosine, Squared Cosine, Raised Cosine, Squared Raised Cosine, and Modulated Sinc. The columns represent the number of primitives used.

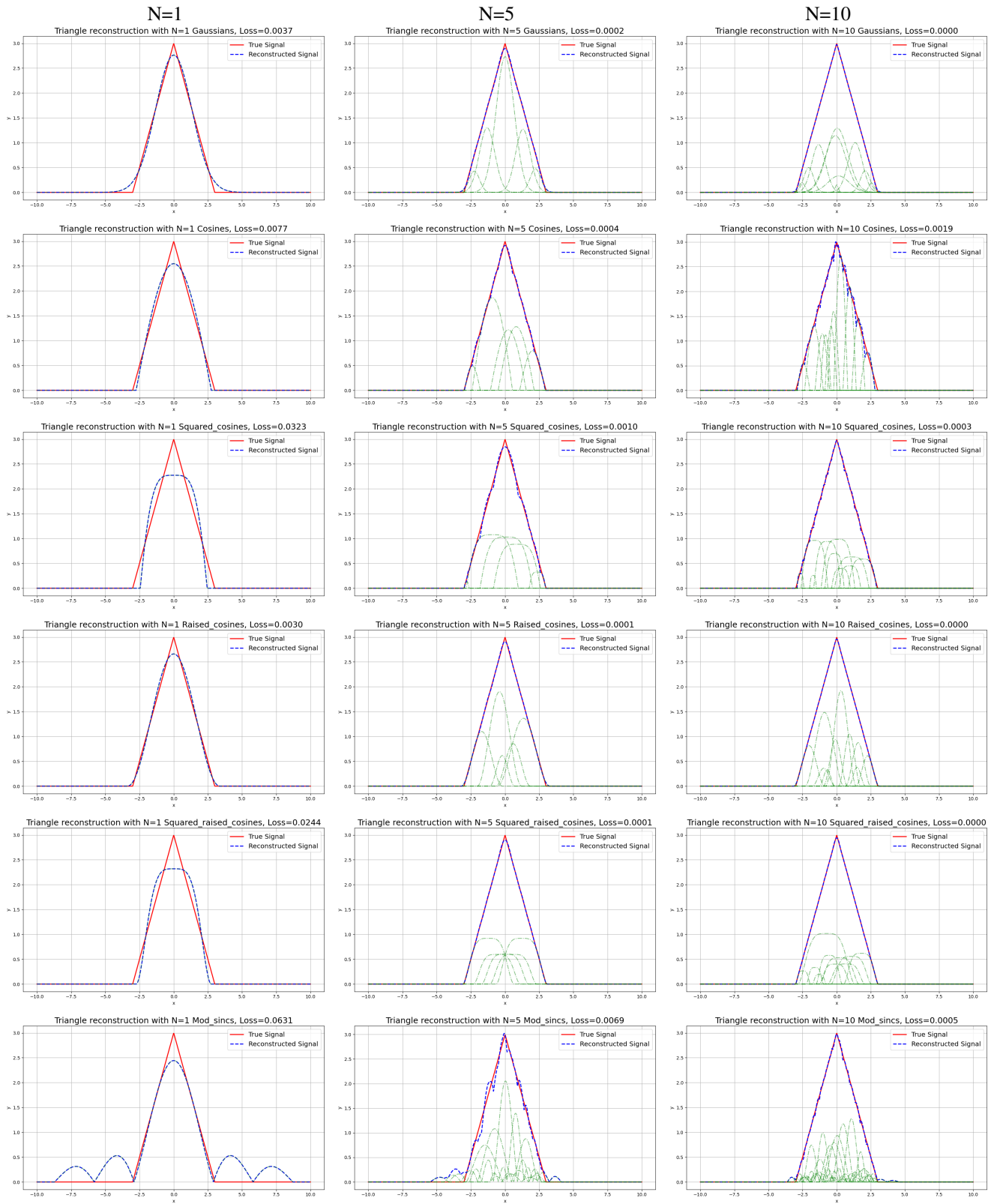


Figure 11. Visualization of 1D simulations for different splatting methods with varying primitives (N=1, N=5, N=10) for a triangle pulse. Each row corresponds to a specific splatting method: Gaussian, Cosine, Squared Cosine, Raised Cosine, Squared Raised Cosine, and Modulated Sinc. The columns represent the number of primitives used.

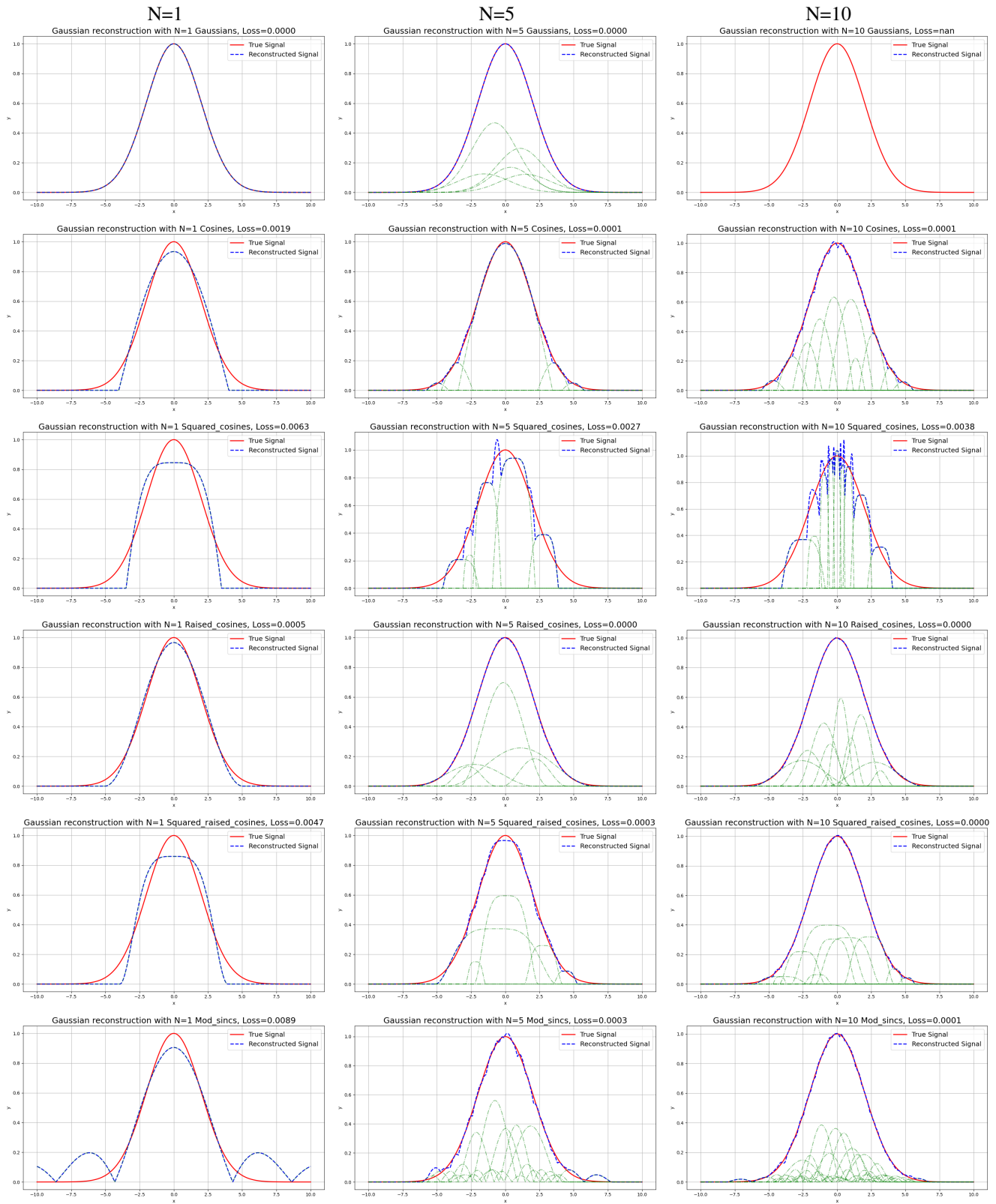


Figure 12. Visualization of 1D simulations for different splatting methods with varying primitives (N=1, N=5, N=10) for a Gaussian. Each row corresponds to a specific splatting method: Gaussian, Cosine, Squared Cosine, Raised Cosine, Squared Raised Cosine, and Modulated Sinc. The columns represent the number of primitives used.

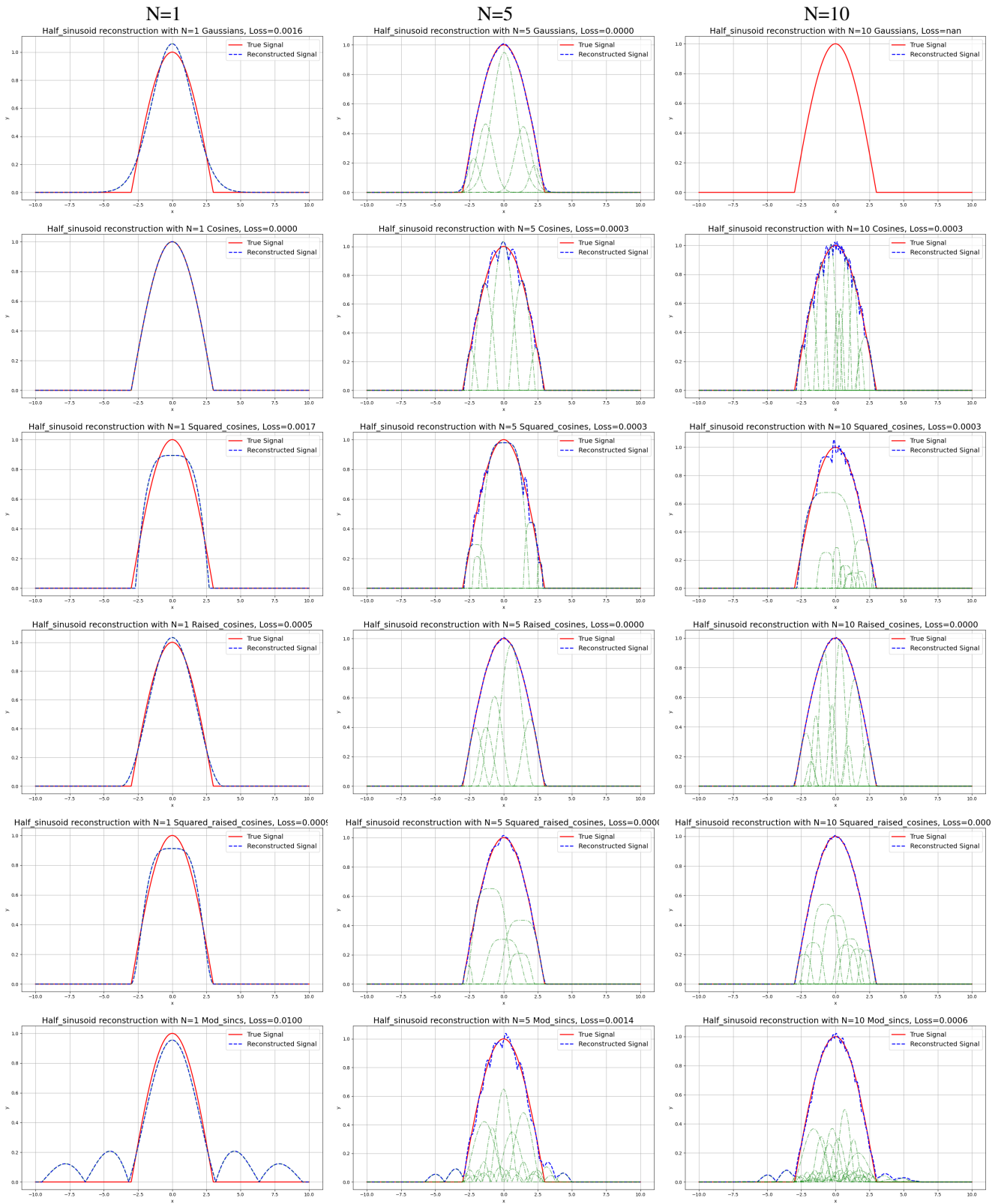


Figure 13. Visualization of 1D simulations for different splatting methods with varying primitives ($N=1$, $N=5$, $N=10$) for a half-sinusoid single pulse. Each row corresponds to a specific splatting method: Gaussian, Cosine, Squared Cosine, Raised Cosine, Squared Raised Cosine, and Modulated Sinc. The columns represent the number of primitives used.

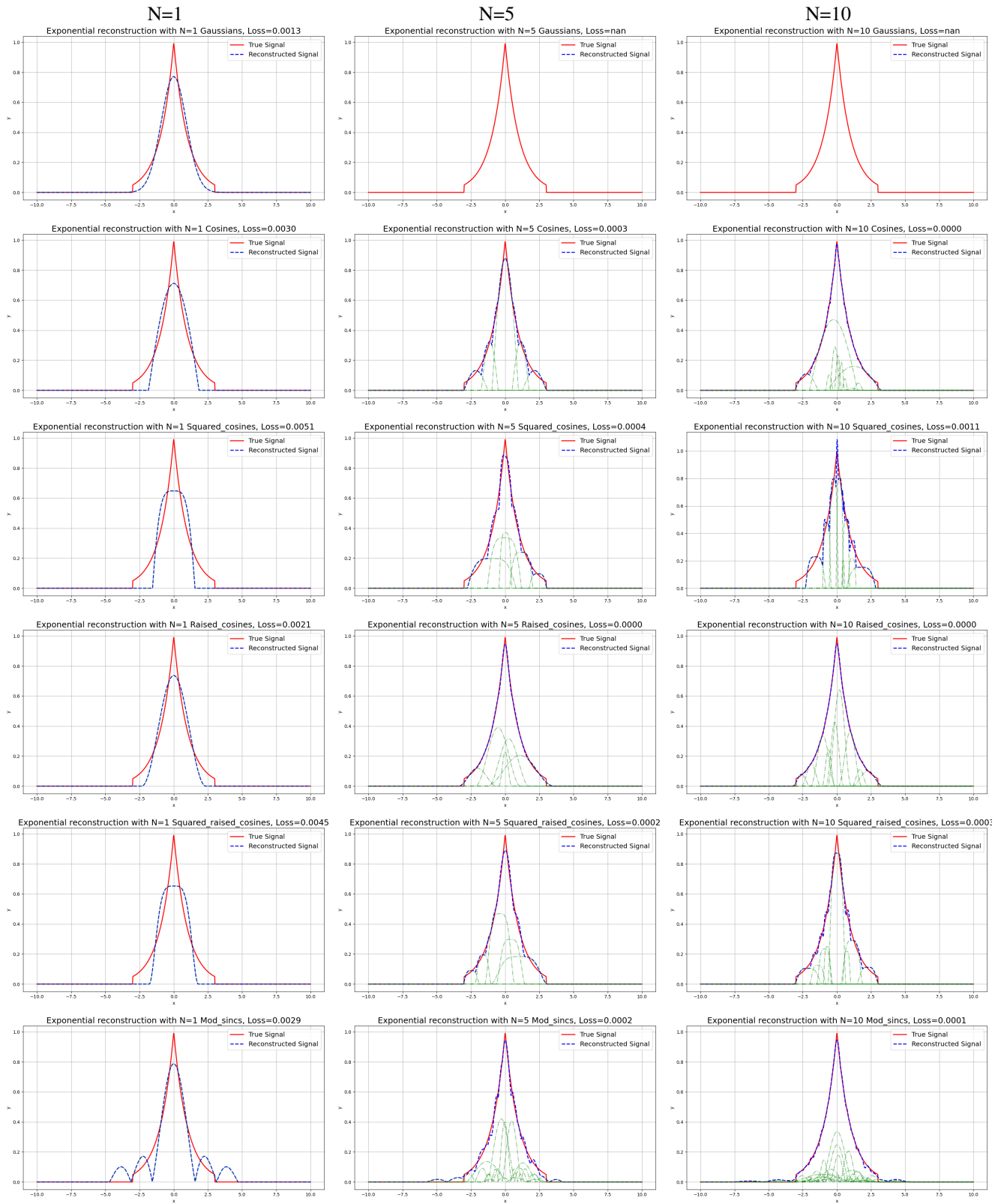


Figure 14. Visualization of 1D simulations for different splatting methods with varying primitives ($N=1$, $N=5$, $N=10$) for a sharp exponential pulse. Each row corresponds to a specific splatting method: Gaussian, Cosine, Squared Cosine, Raised Cosine, Squared Raised Cosine, and Modulated Sinc. The columns represent the number of primitives used.

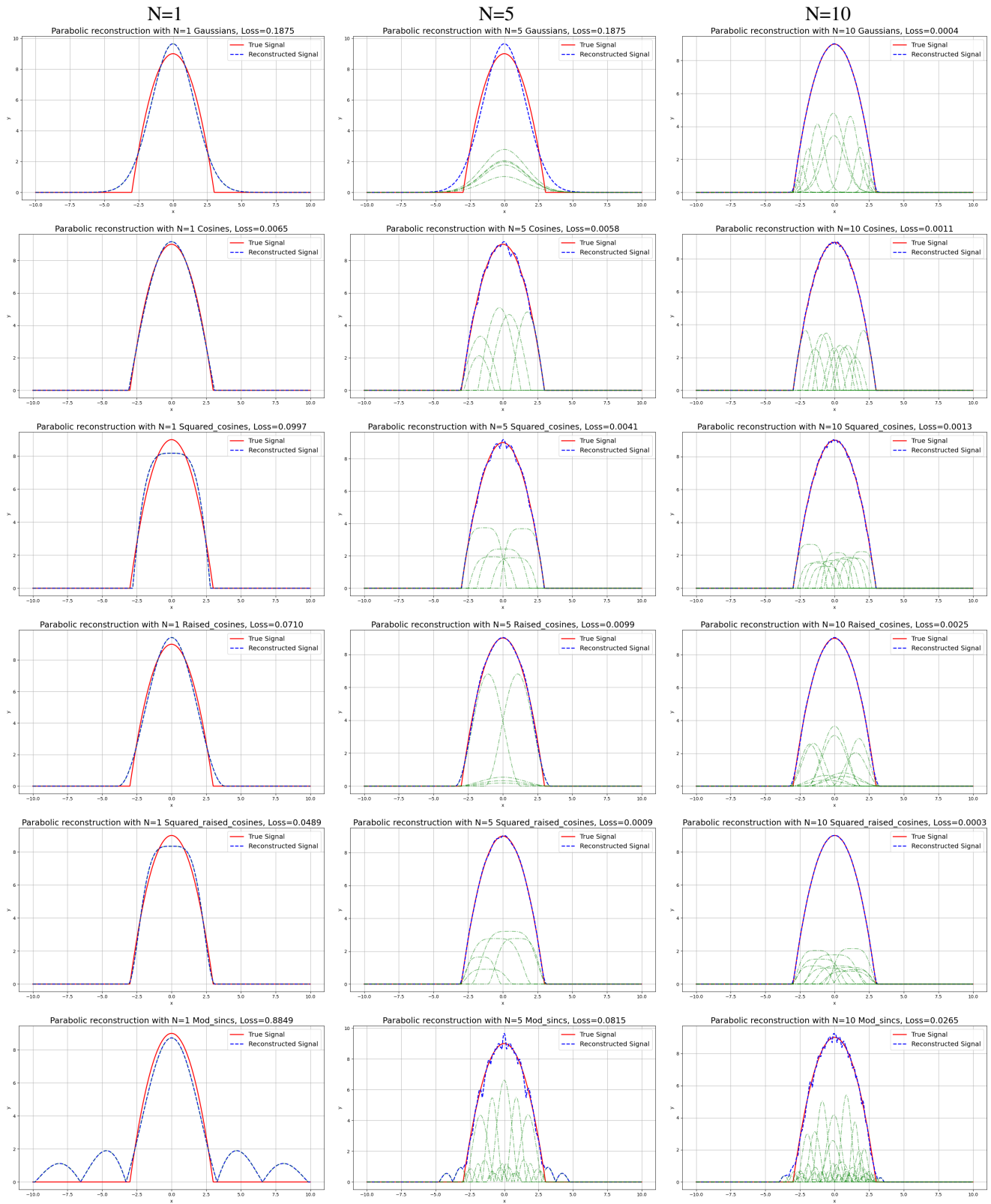


Figure 15. Visualization of 1D simulations for different splatting methods with varying primitives (N=1, N=5, N=10) for a parabolic pulse. Each row corresponds to a specific splatting method: Gaussian, Cosine, Squared Cosine, Raised Cosine, Squared Raised Cosine, and Modulated Sinc. The columns represent the number of primitives used.

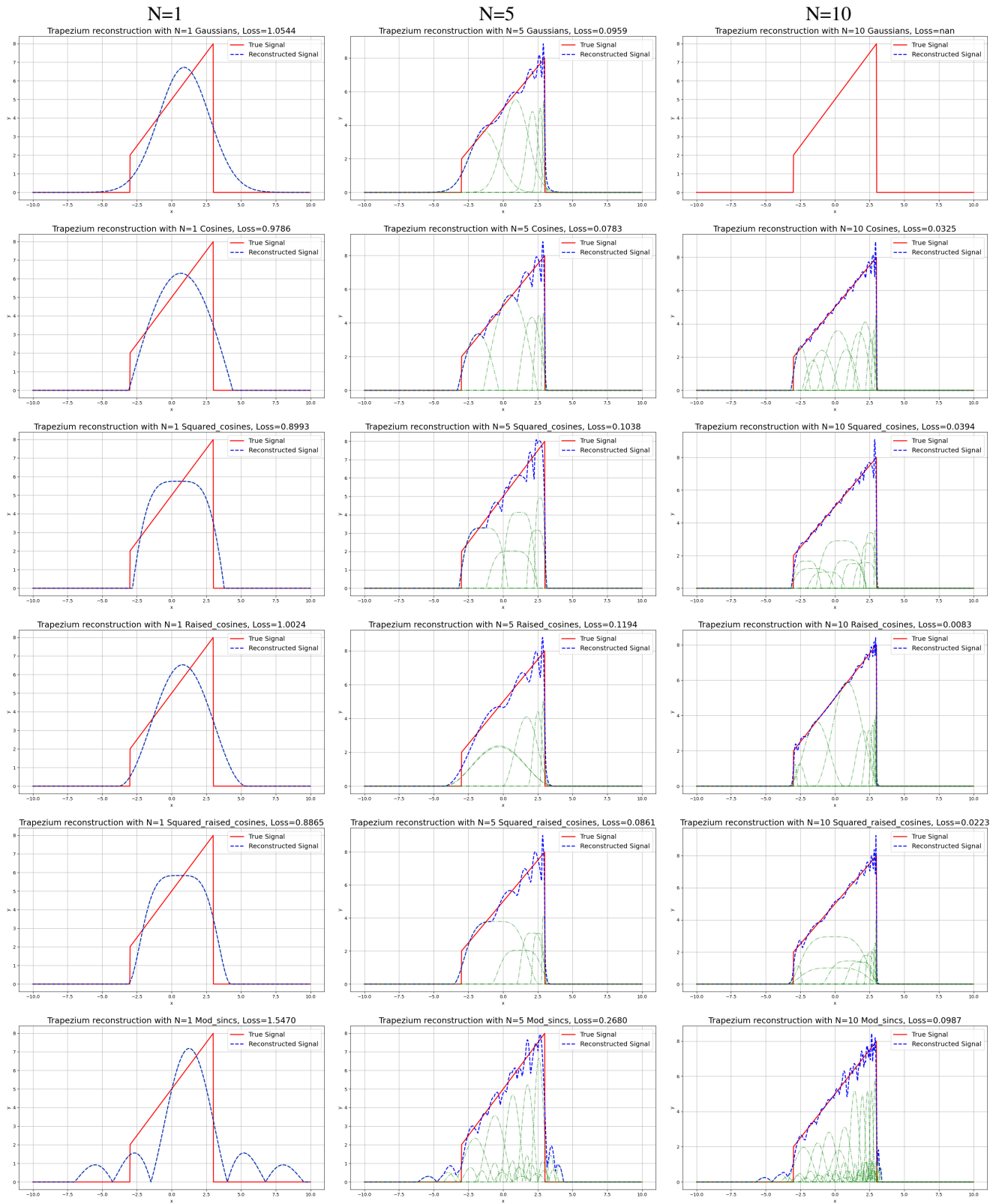


Figure 16. Visualization of 1D simulations for different splatting methods with varying primitives (N=1, N=5, N=10) for a trapezoid pulse. Each row corresponds to a specific splatting method: Gaussian, Cosine, Squared Cosine, Raised Cosine, Squared Raised Cosine, and Modulated Sinc. The columns represent the number of primitives used.

Metric	Model	Step	Bicycle	Flowers	Garden	Stump	Treehill	Room	Counter	Kitchen	Bonsai	Mean
PSNR (dB)	3DGS	7k	23.759	20.4657	26.21	25.712	22.09	29.439	27.179	29.213	29.863	25.9525
		30k	25.248	21.519	27.352	26.562	22.554	31.597	29.055	31.378	32.316	27.4509
	3DRCS	7k	23.81	20.52	26.274	25.825	22.09	29.3625	27.261	29.312	29.635	26.0058
		30k	25.222	21.492	27.374	26.542	22.456	31.342	29.032	31.431	31.842	27.4547
	3DHCS	7k	23.037	19.929	25.351	24.821	22.078	29.127	26.837	28.756	29.481	25.4607
		30k	24.369	21.046	26.585	25.937	22.564	31.003	28.782	31.95	31.89	27.0451
	3DSS	7k	23.371	20.177	25.685	25.2	22.134	29.373	27.078	28.88	29.805	25.7447
		30k	24.813	21.2706	26.985	26.262	22.619	31.467	28.982	31.094	32.213	27.3006
	3DIMQS	7k	23.309	19.782	25.669	24.893	21.591	28.986	26.71	28.211	28.132	25.2536
		30k	24.885	20.838	26.838	26.169	22.389	31.185	28.547	30.34	30.173	26.8182
LPIPS	3DGS	7k	0.328	0.422	0.16	0.294	0.418	0.26	0.2455	0.157	0.236	0.2801
		30k	0.211	0.342	0.108	0.217	0.33	0.22	0.202	0.126	0.205	0.2178
	3DRCS	7k	0.3197	0.41	0.156	0.283	0.406	0.257	0.241	0.155	0.231	0.2732
		30k	0.2079	0.334	0.108	0.212	0.324	0.219	0.2	0.126	0.203	0.2148
	3DHCS	7k	0.403	0.458	0.233	0.35	0.46	0.2787	0.256	0.168	0.238	0.3161
		30k	0.281	0.368	0.156	0.26	0.375	0.234	0.208	0.132	0.206	0.2466
	3DSS	7k	0.374	0.444	0.206	0.328	0.444	0.271	0.25	0.164	0.237	0.302
		30k	0.249	0.359	0.135	0.241	0.356	0.229	0.205	0.129	0.206	0.2343
	3DIMQS	7k	0.355	0.462	0.18	0.335	0.443	0.268	0.253	0.17	0.242	0.3008
		30k	0.238	0.281	0.126	0.248	0.358	0.228	0.21	0.134	0.21	0.2258
SSIM	3DGS	7k	0.669	0.523	0.826	0.722	0.586	0.894	0.875	0.903	0.92	0.7686
		30k	0.763	0.6	0.863	0.769	0.633	0.917	.903	0.9256	0.939	0.8125
	3DRCS	7k	0.6735	0.5302	0.8297	0.7283	0.5913	0.8953	0.8786	0.905	0.9214	0.7726
		30k	0.7641	0.6039	0.864	0.7703	0.6325	0.9176	0.906	0.9256	0.94	0.8137
	3DHCS	7k	0.602	0.478	0.771	0.668	0.557	0.883	0.866	0.894	0.915	0.7371
		30k	0.706	0.566	0.827	0.7337	0.61	0.91	0.898	0.92	0.9355	0.7895
	3DSS	7k	0.631	0.498	0.795	0.693	0.571	0.889	0.873	0.899	0.918	0.7508
		30k	0.736	0.583	0.845	0.752	0.623	0.914	0.903	0.923	0.938	0.8008
	3DIMQS	7k	0.637	0.474	0.8	0.678	0.564	0.884	0.862	0.889	0.911	0.7443
		30k	0.739	0.555	0.843	0.742	0.615	0.909	0.894	0.914	0.928	0.7932
Memory (MB)	3DGS	7k	753	503	840	844	502	259	229	358	252	504
		30k	1135	658	950	1024	727	313	250	384	258	633
	3DRCS	7k	789	516	842	879	528	255	238	370	275	521
		30k	1120	668	953	1010	749	343	276	412	279	645
	3DHCS	7k	570	412	630	699	413	211	228	322	211	410
		30k	858	578	739	867	632	256	242	372	245	532
	3DSS	7k	592	424	672	706	396	240	223	364	266	431
		30k	948	586	800	901	602	281	250	393	272	559
	3DIMQS	7k	394	263	484	478	245	153	140	223	149	281
		30k	608	373	518	611	375	182	151	238	153	356
Training time (s)	3DGS	7k	181	160	212	173	163	225	240	265	217	204
		30k	1378	920	1302	1149	1020	1178	1107	1313	949	1146
	3DRCS	7k	193	155	218	182	159	194	205	239	192	193
		30k	1581	995	1400	1292	1098	1087	1010	1247	876	1176
	3DHCS	7k	164	145	199	158	145	217	223	252	210	172
		30k	1103	806	1035	996	848	1002	934	1181	870	975
	3DSS	7k	182	153	202	169	157	233	243	281	185	201
		30k	1324	879	1215	1093	944	1200	1106	1413	1001	1130
	3DIMQS	7k	161	146	186	152	155	238	263	269	223	199
		30k	1004	704	993	842	799	1105	1049	1261	880	960

Table 11. **Performance metrics across various scenes.** Red color denotes best performance, while yellow denotes third-best. Higher values are better for PSNR, SSIM, and lower values are better for LPIPS, Memory, and Training Time. Here we present a detailed breakdown of results for all scenes from Mip-NeRF360 [12] dataset for 7k and 30k iterations. The performance of each model is heavily affected by the nature of the scene. Some values may differ from the main table due to stochastic processes, as these results are from a single instance of a full evaluation experiment series. In contrast, Table 3 presents the mean results averaged across multiple experiments.

Metric	Model	Step	Tanks&Temples			Deep Blending		
			Truck	Train	Mean	DrJohnson	Playroom	Mean
PSNR (dB)	3DGS	7k	23.933	19.795	21.784	27.609	29.354	28.4215
		30k	25.481	22.201	23.771	29.493	29.976	29.6645
	3DRCS	7k	24.026	19.758	21.882	27.437	29.417	28.477
		30k	25.314	22.077	23.6355	29.35	29.981	29.6355
	3DHCS	7k	22.851	19.391	21.071	26.844	28.965	27.9345
		30k	24.561	21.721	23.108	29.003	29.772	29.3875
	3DSS	7k	23.44	19.658	21.589	27.371	29.417	28.394
		30k	25.03	21.973	23.5065	29.414	29.955	29.6645
	3DIMQS	7k	23.3	19.43	21.365	27.279	28.904	28.0915
		30k	24.83	21.856	23.343	29.239	29.769	29.504
LPIPS	3DGS	7k	0.197	0.318	0.2515	0.318	0.284	0.301
		30k	0.144	0.199	0.1725	0.237	0.243	0.24
	3DRCS	7k	0.19	0.312	0.251	0.3178	0.282	0.2999
		30k	0.1423	0.196	0.1661	0.238	0.2435	0.2407
	3DHCS	7k	0.235	0.354	0.2945	0.341	0.298	0.3195
		30k	0.169	0.231	0.2	0.25	0.256	0.253
	3DSS	7k	0.218	0.334	0.276	0.325	0.292	0.3085
		30k	0.159	0.218	0.1885	0.243	0.25	0.2465
	3DIMQS	7k	0.213	0.34	0.2765	0.327	0.292	0.3095
		30k	0.154	0.221	0.1875	0.24	0.247	0.2435
SSIM	3DGS	7k	0.848	0.719	0.7815	0.87	0.894	0.882
		30k	0.88	0.818	0.851	0.903	0.903	0.903
	3DRCS	7k	0.8527	0.7242	0.7884	0.8696	0.8942	0.8819
		30k	0.8818	0.8197	0.8507	0.9015	0.9013	0.9014
	3DHCS	7k	0.813	0.684	0.7485	0.856	0.887	0.8715
		30k	0.858	0.791	0.8245	0.899	0.9	0.8995
	3DSS	7k	0.831	0.704	0.7675	0.866	0.891	0.8785
		30k	0.869	0.803	0.836	0.902	0.902	0.902
	3DIMQS	7k	0.827	0.693	0.76	0.862	0.886	0.874
		30k	0.866	0.795	0.8305	0.902	0.899	0.9005
Memory (MB)	3DGS	7k	406	180	293	462	336	399
		30k	485	257	371	742	412	577
	3DRCS	7k	476	132	304	491	352	421.5
		30k	548	181	364.5	767	446	606.5
	3DHCS	7k	344	145	244.5	355	331	343
		30k	446	230	338	634	417	482.5
	3DSS	7k	355	156	255.5	399	316	357.5
		30k	434	232	333	682	400	541
	3DIMQS	7k	236	114	175	299	197	248
		30k	291	156	223.5	489	239	364
Training time (s)	3DGS	7k	132	112	122	212	176	194
		30k	738	631	684.5	1385	1039	1212
	3DRCS	7k	134	105	119.5	193	162	177.5
		30k	793	660	726.5	1378	1023	1200.5
	3DHCS	7k	114	103	108.5	213	169	191
		30k	604	498	551	1163	947	1055
	3DSS	7k	131	118	124.5	219	176	197.5
		30k	745	659	702	1407	1087	1247
	3DIMQS	7k	129	123	126	216	164	190
		30k	624	602	613	1262	918	1090

Table 12. **Performance metrics across various scenes.** Red color denotes best performance, while yellow denotes third-best. Higher values are better for PSNR, SSIM, and lower values are better for LPIPS, Memory, and Training Time. Here we present a detailed breakdown of results for all scenes from Tanks&Temples [26] and Deep Blending [19] datasets for 7k and 30k iterations. The performance of each model is heavily affected by the nature of the scene. Some values may differ from the main table due to stochastic processes, as these results are from a single instance of a full evaluation experiment series. In contrast, Table 3 presents the mean results averaged across multiple experiments.